

pubs.acs.org/acscatalysis Research Article

# Experimental and Theoretical Characterization of Rh Single Atoms Supported on $\gamma$ -Al<sub>2</sub>O<sub>3</sub> with Varying Hydroxyl Contents during NO Reduction by CO

Alexander J. Hoffman, Chithra Asokan, Nicholas Gadinas, Emily Schroeder, Gregory Zakem, Steven V. Nystrom, Andrew "Bean" Getsoian, Phillip Christopher, and David Hibbitts



Cite This: ACS Catal. 2022, 12, 11697-11715



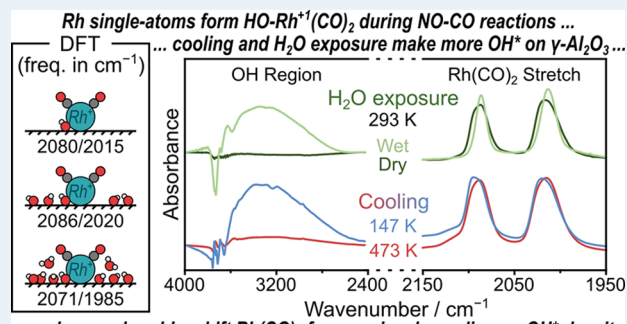
ACCESS I

III Metrics & More

Article Recommendations

Supporting Information

**ABSTRACT:** Oxide-supported Rh catalysts are important components of commercial three-way catalysts for pollution abatement. Despite their universal application, many mysteries remain about the active structure of Rh on oxide supports as these materials often contain a mixture of nanoparticles and single-atom Rh species on the same support, even after aging. Probe molecule Fourier transform infrared (FTIR) spectroscopy in this work shows that atomically dispersed Rh on  $\gamma$ -Al<sub>2</sub>O<sub>3</sub> prefer to strongly bind CO when exposed to NO and CO mixtures and that light-off of NO reduction occurs at temperatures similar to CO desorption, suggesting that the first and rate-determining step in NO—CO reactions may be the desorption of CO from single-atom Rh dicarbonyl complexes, Rh(CO)<sub>2</sub>. Two sets



... and can red- or blueshift Rh(CO)<sub>2</sub> frequencies depending on OH\* density.

of symmetric and asymmetric stretching frequencies associated with distinct  $Rh(CO)_2$  species are observed in FTIR spectra at 2084/2010 and 2094/2020 cm<sup>-1</sup>. During temperature ramps, the latter pair of bands at 2094/2020 cm<sup>-1</sup> converts to the 2084/2010 cm<sup>-1</sup> bands at 463 K before all symmetric and asymmetric bands disappear at 573 K. Bands then appear in the range of 1975–1985 cm<sup>-1</sup> associated with Rh monocarbonyl, Rh(CO), species upon the disappearance of the 2084/2010 cm<sup>-1</sup> bands, suggesting that CO desorbs sequentially from  $Rh(CO)_2$  by forming Rh(CO) intermediates. Combined DFT and FTIR experiments suggest that local OH coverage on the  $\gamma$ -Al<sub>2</sub>O<sub>3</sub> surface distinguishes the two  $Rh(CO)_2$  species: the higher frequency species resides on a less hydroxylated region and migrates to a more hydroxylated region at higher temperatures, causing the CO vibrational frequency to decrease by ~10 cm<sup>-1</sup>. CO desorption occurs from this  $Rh(CO)_2$  structure with high local OH coverage, consistent with the DFT predicted trend of CO binding energies. Because of the coincidence of CO desorption with the light-off of NO reduction, local support hydroxylation of atomically dispersed  $Rh_1/\gamma$ -Al<sub>2</sub>O<sub>3</sub> catalysts likely affects both the Rh structure after CO desorption and the kinetics of NO reduction, studies of which are enabled by the  $Rh(CO)_2$  model developed here.

**KEYWORDS**: NO<sub>x</sub> reduction, three-way catalyst, alumina, single-atom catalyst, rhodium

# 1. INTRODUCTION

Three-way catalysts (TWCs) in catalytic converters have reduced  $NO_x$  emissions by 68% since 1980, after their commercial introduction in 1975.  $^1$   $NO_x$  species are reduced by  $H_2$ , CO,  $NH_3$ , or uncombusted hydrocarbons in engine effluent streams, ideally to form  $N_2$  and  $CO_2$ , but reduction can also produce undesirable  $N_2O$  or  $NH_3$ . Despite significant improvements, TWCs do not sufficiently reduce  $NO_x$  compounds at low temperatures during engine startup (<600 K). As such, TWCs remain actively studied to continue their improvement and reduce emissions. Rh is particularly important because of its high activity for  $NO_x$  reduction with CO and uncombusted hydrocarbons as reductants compared to other Pt-group metals present in TWC, high are more active for  $NO-H_2$  reactions.

TWC wash coats typically contain less than 0.5 wt % Rh, yielding a mixture of Rh structures (and potential active sites) including small Rh nanoparticles and single atoms (Rh<sub>1</sub>) on oxide supports. Additionally, Rh clusters can reversibly disperse into single atoms and re-agglomerate via Ostwald ripening at moderate temperatures. These dispersal-ripening processes are facilitated and accelerated by strong interactions between NO and CO reactants and single metal atoms on oxide supports, and more recent studies have

Received: June 9, 2022 Revised: August 12, 2022 Published: September 12, 2022





illustrated that  $\mathrm{Rh}_1$  speciation on  $\mathrm{TiO}_2$  depends on the gas composition and operating conditions. The mobility of metal atoms during restructuring processes leads to a dynamic distribution of local active site environments under reaction conditions, which complicates rigorous analyses of their catalytic properties but may partly explain why Rh extended surfaces and large supported Rh particles behave differently than low-loading oxide-supported Rh. Therefore, analyzing the behavior of atomically dispersed Rh is required, in addition to studying Rh particles, to understand  $\mathrm{NO}_x$  reduction in catalytic converters where reactions could occur on Rh nanoparticles, single atoms, or both.

Catalysts solely comprising Rh<sub>1</sub> species (within detection limits) have been synthesized in our prior work on  $\gamma$ -Al<sub>2</sub>O<sub>3</sub>. These Rh<sub>1</sub> species selectively produce NH<sub>3</sub> (an undesired byproduct of NOx reduction that contributes to atmospheric particulate formation)<sup>23</sup> during NO reduction in the presence of H<sub>2</sub>O, while nanoparticles more selectively produce N<sub>2</sub> (0.05-5 wt % Rh/ $\gamma$ -Al<sub>2</sub>O<sub>3</sub> and Rh/CeO<sub>2</sub>, 373-623 K, 0.5 kPa CO, 0.1 kPa NO, 0-2% H<sub>2</sub>O).<sup>21,24</sup> The structure of Rh<sub>1</sub> species dispersed on γ-Al<sub>2</sub>O<sub>3</sub> has been investigated in prior work using both theory and experiment, but none have identified the precise structure of the single Rh atoms in conditions relevant to NO, reduction and the effects of surface hydroxylation on their characteristics. 10-13,21,25-28 Probe molecule Fourier transform infrared (FTIR) spectroscopy can help identify these Rh structures and reveal their bonding geometries to reactants—in this case, CO and NO. Early CO probe-molecule FTIR studies of Rh<sub>1</sub>/Al<sub>2</sub>O<sub>3</sub> (0.2–2.2 wt %) identified stretching frequencies characteristic of Rh gem-dicarbonyl structures—Rh(CO)2—with symmetric and asymmetric vibrations near 2090 and 2020 cm<sup>-1</sup>, respectively, that did not vary in frequency with CO\* coverage. [1-13,27,2] Moreover, these IR bands disappeared simultaneously during CO desorption, indicating that the bands were associated with the same species. These studies suggested that the Rh was likely in a +1 oxidation state based on the stoichiometry, X-ray photoelectron spectroscopy (XPS), <sup>13</sup> and extended X-ray absorption fine structure (EXAFS) data. 13,25,26

The γ-Al<sub>2</sub>O<sub>3</sub> surface has many local environments to host supported Rh species. Undercoordinated edge sites on γ-Al<sub>2</sub>O<sub>3</sub> particles can be critical for some chemistries, such as ethanol dehydration.<sup>30–33</sup> These edges may also border different facets that are heterogeneously distributed on the  $\gamma$ -Al<sub>2</sub>O<sub>3</sub> surface; previous microscopy studies have shown that \( \gamma - Al\_2 O\_3 \) facet sizes approach the nanometer scale on some particles.<sup>34</sup> Theoretical studies have suggested the existence of an OH ligand on a Rh<sup>+1</sup>(CO)<sub>2</sub> species supported on  $\gamma$ -Al<sub>2</sub>O<sub>3</sub>; <sup>10</sup> however, such studies did not account for a range of possible OH concentrations on the surface or the effects of changing Rh oxidation states through interactions with other ligands or compare calculations with experimental characterization data. OH groups on the surface of  $\gamma$ -Al<sub>2</sub>O<sub>3</sub> vary in concentration and structure as conditions change according to density functional theory (DFT) calculations of a  $\gamma$ -Al<sub>2</sub>O<sub>3</sub> model derived from dehydrated boehmite, 35-39 and thermogravimetric and surface area analyses suggest that average coverages can range from 8 to 12 OH nm<sup>-2</sup> at the temperatures relevant to CO desorption (573–673 K).<sup>40,41</sup> Neighboring OH may also form hydrogen bonding networks: at high coverage, densely packed OH can form ice-like regions on the support, 42 and OH gathered in surface depressions can form nest-like structures where water can accumulate, 43,44 similar to H-bond networks near silanol

nests on zeolites.  $^{45-50}$  Furthermore, IR bands associated with hydroxyl groups at 3679 and 3735 cm $^{-1}$  decrease when CO is introduced to a 2.2 wt % Rh/ $\gamma$ -Al $_2$ O $_3$  sample while symmetric and asymmetric Rh(CO) $_2$  peaks grow, indicating that particular OH groups are displaced or consumed during the dissolution and oxidation of Rh clusters to Rh $^{+1}$ (CO) $_2$ .  $^{28,51}$  Interestingly, exposing the Rh/ $\gamma$ -Al $_2$ O $_3$  to NH $_3$  mitigates this Rh dispersal process by bonding to  $\gamma$ -Al $_2$ O $_3$  hydroxyl groups.  $^{52}$  A better understanding of the role of OH groups in the behavior and structure of these Rh $_1$  species is critical to studying these active sites for NO $_x$  reduction.

Rh atoms are likely deposited on several facets and in different OH environments during synthesis but can become mobile and likely reconstruct on γ-Al<sub>2</sub>O<sub>3</sub> depending on changing surface environments during catalyst treatment and reaction conditions. CO-induced restructuring of atomically dispersed Rh<sub>1</sub>/ $\gamma$ -Al<sub>2</sub>O<sub>3</sub> relies on the migration of Rh(CO)<sub>2</sub> across the  $\gamma$ -Al<sub>2</sub>O<sub>3</sub> surface to produce spatially isolated Rh species or to induce their re-agglomeration. <sup>11–16</sup> Indeed, sintering of atomically dispersed Rh can be suppressed by anchoring organic ligands to limit Rh mobility. 53,54 Rh cluster fragmentation occurs on the order of seconds when exposed to CO near ambient temperature, according to time-resolved EXAFS, with a low 17 kJ mol<sup>-1</sup> barrier to form Rh(CO), from adjacent Rh atoms. 14 DFT studies of Pd<sub>1</sub> diffusion indicated an activation barrier between 15 and 72 kJ mol<sup>-1</sup> for diffusion across dehydrated and hydrated (110)  $\gamma$ -Al<sub>2</sub>O<sub>3</sub> surfaces, respectively.<sup>55</sup> The high mobility of Rh atoms may allow them to traverse the \( \gamma - Al\_2 O\_3 \) surface and sample a range of surface facets, local adsorbate environments, and hydroxyl densities at relevant desorption and reaction conditions until finding a stable bonding geometry.

Here, we use a combination of spectroscopic and theoretical methods to rigorously analyze the structure, adsorption behavior, and spectroscopic properties of Rh<sub>1</sub> supported on γ-Al<sub>2</sub>O<sub>3</sub> under conditions relevant for NO reduction by CO. We show that  $Rh(CO)_2$  is the preferred structure when single Rh atoms are exposed to NO reduction reaction conditions (478 K, 0.5 kPa CO and 0.1 kPa NO, Ar balance, 1 bar total). DFT-calculated vibrational frequencies of adsorbed CO\* most closely match experiments when Rh(CO)<sub>2</sub> is coordinated to a single OH group—compared to other possible ligands containing H and O-on the \gamma-Al2O3 surface at a variety of water coverages. Furthermore, FTIR spectroscopy reveals shifts in CO frequency that suggest the local Rh environment changes during temperature-programmed desorption (TPD), which is expected for a mobile species on a heterogeneous support like  $\gamma$ -Al<sub>2</sub>O<sub>3</sub>. We conclude that local OH coverage around Rh(CO)<sub>2</sub> alters the gem-dicarbonyl symmetric and asymmetric stretching frequencies and CO binding energies, suggesting that this factor is relevant for CO desorption and subsequent reactions of NO and CO on atomically dispersed  $Rh_1/\gamma$ - $Al_2O_3$ .

# 2. MATERIALS AND METHODS

**2.1. Computational Methods and Models.** Periodic DFT calculations were completed using the Vienna Ab initio Simulation Package<sup>\$6-59</sup> in the computational catalysis interface (CCI). The revised Perdew–Burke–Ernzerhof (RPBE) form of the generalized gradient approximation (GGA) was used for most calculations, <sup>61,62</sup> and planewaves were composed of projector augmented waves (PAW) <sup>63,64</sup> with an energy cutoff of 400 eV. Select structures were

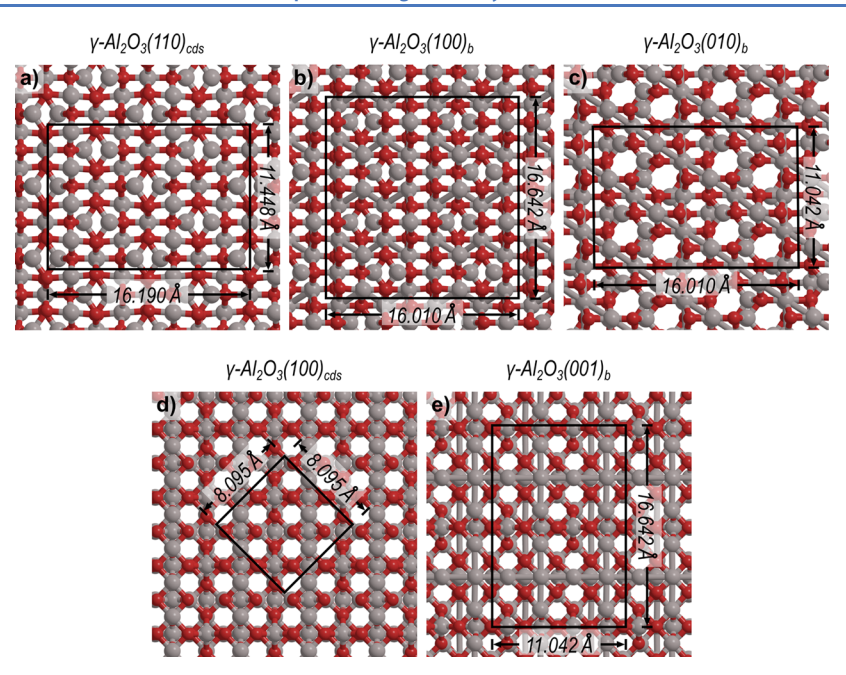


Figure 1. Top views of the (a)  $(110)_{cds}$  surface and the corresponding (b)  $(100)_b$  and (c)  $(010)_b$  surfaces and the (d)  $(100)_{cds}$  and corresponding (e)  $(001)_b$  surface models of γ-Al<sub>2</sub>O<sub>3</sub>. Lengths of unit cell vectors are labeled in Å. Additional views are shown in Figure S2 of the Supporting Information.

Table 1. Identities and Unit Cell Parameters of Surface Models from γ-Al<sub>2</sub>O<sub>3</sub> Tested in This Work

boehmite facet	$\gamma$ -Al $_2$ O $_3$ facet $^a$	unit cell parameters $(a \times b \times c)/\text{Å}^b$	$\gamma/^{\circ c}$	supercell
$(100)_{\rm b}$	$(110)_{\rm cds}$	$8.321 \times 8.005 \times 21.851$	90.000	$2 \times 2 \times 1$
$(010)_{\rm b}$	$(110)_{\rm cds}$	$8.005 \times 5.521 \times 17.066$	90.588	$2 \times 2 \times 1$
$(001)_{b}$	$(100)_{\rm cds}$	$5.521 \times 8.321 \times 16.358$	90.000	$2 \times 2 \times 1$

<sup>&</sup>lt;sup>a</sup>The most similar surface of cds materials. <sup>b</sup>The c-vector for each facet is perpendicular to the exposed surface and includes the 10 Å of vacuum. <sup>c</sup>α and  $\beta$  values are 90.00° for all surface models.

optimized a second time using the Heyd–Scuseria–Ernzerhof (HSE06) hybrid exchange–correlation functional. S5-68 Structures were optimized using a multi-step process implemented in CCI. Wavefunctions were converged to within  $10^{-4}$  in the first step with forces calculated using a fast Fourier transform (FFT) grid of 1.5× the planewave cutoff. Wavefunctions were optimized in the second step within  $10^{-6}$  eV and with an FFT grid 2× the planewave cutoff. Structures were optimized such that forces on all atoms were <0.05 eV Å $^{-1}$  in both steps. Partial charges were estimated using quasiatomic minimum basis orbitals (QUAMBO). Gas-phase species were modeled in  $18 \times 18 \times 18$  Å unit cells surrounded by vacuum with spin polarization for species with partially occupied orbitals in their valence shells.

The  $\gamma$ -Al<sub>2</sub>O<sub>3</sub> model employed here was developed from a bulk structure constructed by modeling the dehydration of boehmite [ $\gamma$ -AlO(OH)] to form  $\gamma$ -Al<sub>2</sub>O<sub>3</sub> (a=5.587 Å, b=8.413 Å, c=8.068 Å;  $\alpha=\gamma=90.00^\circ$ ,  $\beta=90.59^\circ$ ).  $^{35,37-39}$  This approach is necessary because previous cubic defect spinel-like models were less stable in DFT calculations and as-synthesized  $\gamma$ -Al<sub>2</sub>O<sub>3</sub> has low crystallinity, rendering periodic models for DFT difficult to construct from characterization data alone. We illustrate the instability of cubic defect spinel models during DFT calculations and compare the boehmite-derived model and a cubic defect spinel model (a=b=c=7.887 Å;  $\alpha=\beta=\gamma=90.00^\circ$ ) in Section S2 of the Supporting Information. After optimizing the bulk unit cell parameters of the boehmite-derived  $\gamma$ -Al<sub>2</sub>O<sub>3</sub> model (a=5.521 Å, b=8.321

Å, c = 8.005 Å;  $\alpha = \gamma = 90.00^{\circ}$ ,  $\beta = 90.588^{\circ}$ ), surface formation energies were calculated for the (100), (010), and (001) surfaces of this dehydrated boehmite surface (Figure 1 and Table 1). We note that in this work we retain the Miller indices for the boehmite from which this  $\gamma$ -Al<sub>2</sub>O<sub>3</sub> model was derived because its (100) and (010) surfaces both resemble the (110) facet of γ-Al<sub>2</sub>O<sub>3</sub>, although they differ in their structures and unit cell sizes (Figure 1).<sup>39</sup> These surfaces have distinct Miller indices from cubic defect spinel γ-Al<sub>2</sub>O<sub>3</sub> models, as shown in Figure 1 and discussed in Section S2 of the Supporting Information. We denote the surfaces of the models we use in this study with a "b" subscript to show that they are derived from dehydrated boehmite [e.g.,  $(010)_b$ ], while indices for the typical cubic defect spinel structure are denoted with a "cds" subscript, including when describing experimental characterization data [e.g., (110)<sub>cds</sub>, which most closely matches (100)<sub>b</sub> and  $(010)_b$ ]. A 10 Å vacuum layer was added above the surface. Supercells were used for each surface to reduce lateral interactions between adsorbates on Rh/\gamma-Al2O3 systems, as shown in Table 1. Calculations using the RPBE functional for  $\gamma$ -Al<sub>2</sub>O<sub>3</sub> and Rh/ $\gamma$ -Al<sub>2</sub>O<sub>3</sub> systems sampled the Brillouin zone using a  $\Gamma$ -centered 2  $\times$  2  $\times$  1 K-point mesh and were performed with spin polarization. Calculations performed with HSE06 only sampled the  $\Gamma$ -point of the Brillouin zone.

We calculate binding energies for  $H_2O^*$  or  $OH^*/H^*$  pairs on  $\gamma$ -Al<sub>2</sub>O<sub>3</sub> surfaces ( $\Delta E_{W,n}$ ) with respect to gas-phase  $H_2O(g)$ 

$$\Delta E_{W,n} = E_{W,n} - E_{W,n-1} - E_{W(g)} \tag{1}$$

where  $E_{\mathrm{W},n}$  is the energy of the most stable configuration of n H<sub>2</sub>O\* (or n OH\*/H\* pairs) on the surface. Similarly, for CO\* on Rh<sub>1</sub>/ $\gamma$ -Al<sub>2</sub>O<sub>3</sub> ( $\Delta E_{\mathrm{CO},n}$ ), differential binding energies were also calculated

$$\Delta E_{\text{CO},n} = E_{\text{Rh}(\text{CO})_n} - E_{\text{Rh}(\text{CO})_{n-1}} - E_{\text{CO}(g)}$$
(2)

where  $E_{Rh(CO)n}$  is the most stable configuration of the Rh single atom with n CO adsorbates. Finally, the binding energy of the entire  $Rh(CO)_2$  complex was calculated using a gas-phase  $Rh(CO)_2$  reference state

$$\Delta E_{\text{Rh(CO)}_2} = E_{\text{Rh(CO)}_2/\text{Al}_2\text{O}_3} - E_{\text{Al}_2\text{O}_3} - E_{\text{Rh(CO)}_2(g)}$$
(3)

to give insights into the adhesion of these Rh(CO)<sub>2</sub> species to  $\gamma$ -Al<sub>2</sub>O<sub>3</sub>. This gas-phase Rh(CO)<sub>2</sub> structure was calculated with spin polarization, as were  $\gamma$ -Al<sub>2</sub>O<sub>3</sub> and Rh/ $\gamma$ -Al<sub>2</sub>O<sub>3</sub> systems.

Frequency calculations of optimized structures were used to determine zero-point vibrational energies (ZPVE) and rotational, translational, and vibrational enthalpies (H) and free energies (G) at 473 K based on formalisms from statistical mechanics (Section S1, Supporting Information). Translation and rotation of adsorbates on surfaces were treated as frustrated motions and modeled as vibrations, while translation and rotation of gas-phase species were treated as ideal, and corresponding translational and rotational partition functions were used to calculate enthalpy

$$H = E_0 + \text{ZPVE} + H_{\text{vib}} + H_{\text{rot}} + H_{\text{trans}} \tag{4}$$

and free energy

$$G = E_0 + \text{ZPVE} + G_{\text{vib}} + G_{\text{rot}} + G_{\text{trans}}$$
 (5)

Frequencies were calculated using a fixed displacement method (two displacements) where all adsorbate atoms (H<sub>2</sub>O\*, H\*, OH\*, Rh, and anything bound to Rh) were displaced. All frequencies below 60 cm<sup>-1</sup> were replaced with 60 cm<sup>-1</sup> in estimations of enthalpy or free energies, consistent with prior work, <sup>6,72,73</sup> because low-frequency vibrations are inaccurately predicted by DFT, but their exclusion would exacerbate errors in computed adsorbate entropies. CO stretch frequencies were scaled based on the gas-phase CO stretching frequency (2143 cm<sup>-1</sup>)<sup>74</sup> and the DFT-calculated CO stretching frequency. For example, the calculated CO frequency is 2102 cm<sup>-1</sup> using the RPBE functional and PAW potentials, and therefore, all calculated frequencies using those methods were scaled by a factor of 1.019. Frequencies were not adjusted when calculating enthalpies and free energies.

**2.2. Experimental Methods.** 2.2.1. Catalyst Synthesis. Atomically dispersed 0.1 and 0.05 wt % Rh catalysts were synthesized using incipient wetness impregnation by dissolving Rh(III) nitrate hydrate precursor [Rh(NO<sub>3</sub>)<sub>3</sub>:xH<sub>2</sub>O, Sigma-Aldrich, CAS: 10139-58-9] in 80 cm³ of high-performance liquid chromatograph-grade water (J.T. Baker, CAS: 7732-18-15) and adding the diluted precursor solution 0.2 cm³ at a time to dry  $\gamma$ -Al<sub>2</sub>O<sub>3</sub> support powder (Sasol, Puralox TH100/150, CAS: 9529248-35-0) in a 10 cm³ ceramic evaporation dish. The mixtures were dried overnight in an oven at 373 K. The catalyst powders were then treated in dry air in a tube furnace at 623 K for 4 h.

2.2.2. Probe Molecule FTIR Spectroscopy. Catalysts were loaded in a Harrick low-temperature reaction chamber mounted inside a ThermoScientific Praying Mantis diffuse reflectance adapter set in a Nicolet iS10 FTIR spectrometer with a mercury cadmium telluride (MCT) detector, and mass flow controllers (Teledyne Hastings) were used to control the

gas flow rates across the reactor bed. Catalysts were pretreated in situ for 0.5 h at 623 K in pure O<sub>2</sub> at 1 bar and subsequently in 10 kPa H<sub>2</sub>/Ar at 373 K in a Harrick reaction chamber for 1 h. FTIR spectra were taken with 12 scans and 0.482 cm<sup>-1</sup> data spacing. IR spectra collected under reaction conditions were taken after samples were pretreated in situ, heated to a reaction temperature of 478 K in flowing Ar, while continuously exposed to flowing 0.1 kPa NO, 0.5 kPa CO, and balance Ar until spectra remained unchanging. CO probe molecule IR spectra were taken after samples were pretreated in situ, brought to the CO adsorption temperature (298 or 423 K) in flowing Ar, exposed to flowing 1 kPa CO in Ar until Rh sites were saturated—indicated when spectra remained unchanging—and purged with Ar. Isotopically labeled CO (>99% <sup>13</sup>CO, <5% <sup>18</sup>O) was used to identify NCO\* by saturating the catalyst with 10 kPa <sup>13</sup>CO and pulsing with 1 kPa NO at 463 K. The predominant Rh species was probed by saturating the catalyst with 0.5 kPa CO prior to exposure to 0.5 kPa CO and 0.1 kPa NO at 463 K and by allowing the catalyst to remain in 0.5 kPa CO and 0.1 kPa NO at 523 K for 1.5 h. Cryogenic temperatures were achieved by adding liquid N<sub>2</sub> to a dewar attached to the reaction chamber. The area of the H-bonding OH region (3600-2500 cm<sup>-1</sup>) was computed with a linear baseline between 4000 and 2400 cm<sup>-1</sup>, and the full width at half max (fwhm) was taken as the width of each CO peak at half the distance from peak maximum to a linear baseline between the end points of the peak. In experiments where the material was exposed to variable water concentrations, the COsaturated Rh catalyst was exposed to a water-saturated Ar stream by diverting the Ar through a water bubbler at ambient temperature and pressure prior to entering the reaction chamber.

TPD measurements were executed by heating the sample in Ar at a rate  $(\beta)$  of 0.33 K s<sup>-1</sup> (20 K min<sup>-1</sup>) until all CO desorbed while taking spectra continuously. The rate of band intensity loss was traced using the change in peak areas of deconvoluted spectra, integrated and fit using Origin by fixing constant peak fwhm and positions. We estimate the CO binding energy range by solving the following form of the Redhead analysis equation numerically in MATLAB, similar to our prior work<sup>53</sup>

$$\ln\left(\frac{\beta}{k_{\rm B}T_{\rm P}^2}\right) = \frac{-E}{k_{\rm B}T_{\rm P}} + \ln\left(\frac{A}{E}\right) \tag{6}$$

where E is the binding energy,  $T_{\rm P}$  is the peak desorption temperature,  $k_{\rm B}$  is the Boltzmann constant,  $\beta$  is the temperature ramp rate (0.33 K s<sup>-1</sup>), and A is the pre-exponential factor. When estimating the CO binding energy without an entropic barrier ( $\Delta S=0$ ), we use a preexponential factor (A) of  $10^{13}$ , based on a previous analysis of flat Rh surfaces where single molecular desorption occurs. He pre-exponential factor (A) used is  $6 \times 10^{11}$  s<sup>-1</sup> for a CO entropic desorption barrier of 52 J mol K<sup>-1</sup> from Rh(CO)<sub>2</sub>, as calculated in a previous work. From these energies, we can estimate desorption enthalpy,  $\Delta H$ 

$$\Delta H = E - RT_{\rm P} \tag{7}$$

where R is the ideal gas constant.

2.2.3. NO Reduction Light-Off Experiment. "Light-off" experiments were performed to test the reactivity of atomically dispersed Rh catalysts, where the reactor was heated at a

constant rate under reactive environments from ambient temperature, mimicking engine start-up conditions. Catalysts were diluted with purified SiO<sub>2</sub> (Sigma-Aldrich, CAS: 84878) to 2 (mg Rh) g<sub>cat</sub><sup>-1</sup> in a home-built, temperature-controlled reactor system with mass flow controllers (Teledyne Hastings) to precisely control CO, NO, H2O, and Ar gas flow concentrations. After pretreatment identical to that used before CO FTIR characterization, catalysts were heated by  $0.0833 \text{ K s}^{-1} \text{ from } 293 \text{ to } 723 \text{ K, while } 4.17 \text{ cm}^3 \text{ s}^{-1} \text{ of } 0.5 \text{ kPa}$ CO and 0.1 kPa NO in Ar gas (1 bar total) flowed over a packed bed. Gas-phase product compositions were identified by flowing outlet effluent through a Thermo Scientific Antaris IGS 2 m Gas Cell set in a Nicolet iS10 FTIR spectrometer with an MCT detector and using OMNIC Series Software to take 5 spectral scans every 10 s at high 0.5 resolution and 0.241 cm<sup>-1</sup> data spacing. Reactants and products were calibrated with the TQ Analyst Pro Edition Software to identify established spectral signatures of known mixtures of CO, NO, N<sub>2</sub>O, NH<sub>3</sub>, CO<sub>2</sub>, and H<sub>2</sub>O in Ar at set pressure and temperature.

#### 3. RESULTS AND DISCUSSION

# 3.1. CO-NO Mixtures over Atomically Dispersed Rh.

Designing structural models that coincide with characterization data of working catalytic active sites first requires the identification of structural elements present under reaction conditions. In situ FTIR provides insights into the Rh structure during NO reduction by CO and the predominant adsorbate that saturates the active sites. Upon exposure to conditions of realistic TWC operation, 0.5 kPa CO and 0.1 kPa NO (5000 and 1000 ppm, respectively) at 478 K, atomically dispersed Rh exists predominantly as Rh(CO)<sub>2</sub> with characteristic frequencies at 2084 and 2012 cm<sup>-1</sup> and without peaks associated with NO\* on Rh expected in the range of 1700–1800 cm<sup>-1</sup> (Figure 2). <sup>11,12,25,27</sup> Additionally, exposing a CO-saturated catalyst to

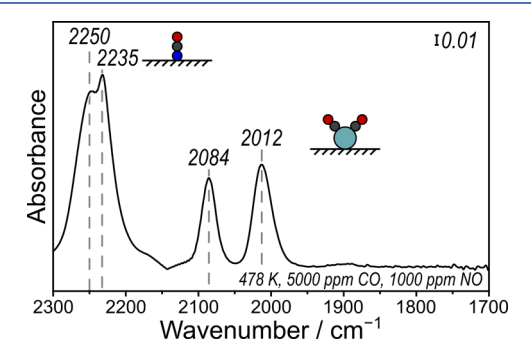


**Figure 2.** In situ IR spectra of 0.1 wt % Rh/ $\gamma$ -Al<sub>2</sub>O<sub>3</sub> during NO—CO reactions at 478 K for 600 s (0.5 kPa CO and 0.1 kPa NO, Ar balance, 1 bar total). Inset cartoons show the assigned species associated with the observed bands where O is red, C is gray, N is blue, and Rh is cyan.

the mixture of NO and CO does not cause the intensity of Rh(CO)<sub>2</sub> bands to decrease (Figure S2a, Supporting Information). These data indicate that atomically dispersed Rh is exclusively coordinated to CO, rather than NO, at conditions similar to those in automotive exhaust treatment. This preference for CO\* on Rh<sub>1</sub> contrasts with Rh nanoparticles and surfaces, where NO adsorbs more strongly than CO, resulting in NO\*-saturated Rh surfaces under similar conditions.<sup>77</sup> The differences in the preferred most abundant surface intermediates (MASI) between Rh<sub>1</sub> and Rh nano-

particles may contribute to differences in their selectivities and reactivities during  $\mathrm{NO}_x$  reduction. Therefore, we focus on  $\mathrm{Rh}_1$  coordinated to  $\mathrm{CO}^*$  in this study to guide DFT-calculated structures with experimental characterization data. The models developed herein can then be used to study the mechanistic differences between these active site structures more rigorously in future work.

Notably, other peaks appear at 2250 and 2235 cm<sup>-1</sup> during exposure of the catalysts to CO and NO, which are assigned to adsorbed NCO\* species on  $\gamma$ -Al<sub>2</sub>O<sub>3</sub>. The shoulders at 2130 and 2170 cm<sup>-1</sup> in Figure 2 correspond to the P and R branches of gas-phase CO, respectively. These features are visible in the IR spectrum of the 0.05 wt %  $Rh/\gamma$ - $Al_2O_3$  catalyst during CO exposure in the absence of NO (Figure S2a, Supporting Information), but they do not appear in spectra of the catalysts that had been exposed to the NO/CO mixture and then purged with Ar (Figure S2b, Supporting Information). IR spectra of the 0.05 wt % Rh/ $\gamma$ -Al<sub>2</sub>O<sub>3</sub> sample show similar but shifted bands when exposed to <sup>12</sup>CO and isotopically labeled <sup>13</sup>CO mixed with NO (Figure S2b, Supporting Information). Both the sets of symmetric and asymmetric Rh(CO)<sub>2</sub> stretches, and the features near 2230-2250 red-shift by ~50 cm<sup>-1</sup>, indicating that each is associated with species containing C, which further indicates that the 2230–2250 cm<sup>-1</sup> bands are caused by NCO\*. Prior work<sup>21,78–81</sup> has indicated that such NCO\* species can spill over onto the γ-Al<sub>2</sub>O<sub>3</sub> support once formed during NO reduction by CO on Rh/ $\gamma$ -Al<sub>2</sub>O<sub>3</sub>, which is confirmed in this work by the slow growth of these features without loss of Rh(CO)<sub>2</sub> in IR spectra collected at 523 K (Figure S2c, Supporting Information). Al<sub>2</sub>O<sub>3</sub> also favors the formation of NCO\* species more than other more inert materials such as SiO<sub>2</sub> and MgO, 81,82 further indicating the importance of the support in forming and stabilizing these NCO\*. Although these earlier studies used higher weight loadings of Rh, their findings indicate that understanding support effects is crucial to understanding the mechanism of NO<sub>x</sub> reduction on both Rh<sub>1</sub> and nanoparticles. Notably, the precise mechanism by which these NCO\* species form on Rh<sub>1</sub> remains unknown, and additional data are needed to determine the preferred path. While prior studies have suggested that NCO\* can form through N\* on Rh nanoparticles,<sup>78</sup> the same mechanism may not be possible on Rh<sub>1</sub>. Thus, we conclude that NCO\* is adsorbed only on the  $\gamma$ -Al<sub>2</sub>O<sub>3</sub> support, while atomically dispersed Rh species exist almost exclusively as  $Rh(CO)_2$  species under reaction conditions.

Prior studies have indicated that oxide-supported Rh(CO)<sub>2</sub> species are in a +1 oxidation state and are bound to an OH on the surface of the oxide. 20,83,84 We explore different coordinating ligands that lead to different Rh oxidation states using DFT calculations, but we first compare the binding energies of CO and NO to confirm the observed preponderance of Rh(CO)<sub>2</sub> in IR spectra observed below 573 K in Figure 3 in an NO/CO mixture. Electronic binding energies for the first CO are weaker (-268 kJ mol<sup>-1</sup>) than for NO  $(-299 \text{ kJ mol}^{-1})$ , while the second NO binds more weakly  $(-169 \text{ kJ mol}^{-1})$  than the second CO  $(-174 \text{ kJ mol}^{-1})$  when calculated using the RPBE exchange-correlation functional (Figure 3). Previous work has used HSE06 hybrid functionals to improve predictions from GGA functionals for NO binding to single-atom Cu<sup>85–87</sup> and Pd<sup>88</sup> within zeolites because GGĀ functionals overpredict NO binding energies on these cationic metal sites. While Rh differs from Cu and Pd, we repeat these binding energy calculations using HSE06 for comparison to

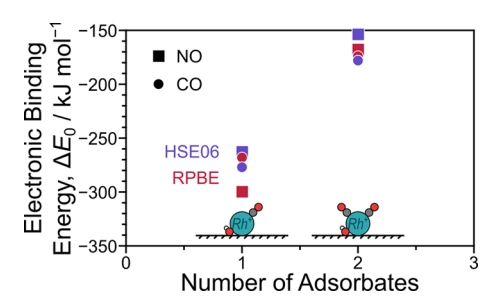


Figure 3. Electronic binding energies ( $\Delta E_0$ ) for CO ( $\bullet$ ) and NO ( $\blacksquare$ ) on an Rh single atom coordinated to an OH ligand on the  $\gamma$ -Al<sub>2</sub>O<sub>3</sub> using the RPBE exchange—correlation functional (red) and the HSE06 exchange—correlation functional (purple).

RPBE for these adsorbates with more complex electronic structures. CO binding energies from HSE06 (-277 and -178 kJ mol<sup>-1</sup>) remain similar to those from RPBE (-268 and -174kJ mol<sup>-1</sup>) for the first and second CO, respectively. In contrast, NO binding energies are much weaker when calculated with HSE06 (-262 and -153 kJ  $mol^{-1}$  for the first and second NO, respectively) than with RPBE (-299 and -167 kJ mol<sup>-1</sup>) (Figure 3). These findings indicate that more accurate computational approaches are needed for molecules with challenging electronic structures like NO and that RPBE is appropriate for CO calculations on these Rh models. Additionally, these data corroborate the experimental observation that Rh single atoms are saturated by CO\* pairs rather than NO\* or CO\*-NO\* mixtures in situ, which is in contrast to the preference of extended Rh surfaces to be saturated by NO\* under similar conditions. 77 While the differences in these computed binding energies are close to DFT error (typically considered  $\pm 10 \text{ kJ mol}^{-1}$ ), their agreement with experimental observations and the change in the binding trends indicate that HSE06 more accurately predicts adsorption behavior on Rh<sub>1</sub>. Based on the absence of any other features between 1700 and 2300 cm<sup>-1</sup> in the in situ IR and initial calculations suggesting the preference for CO rather than NO to adsorb on Rh<sub>1</sub>, we focus on understanding the characteristics of Rh(CO)2 as the catalyst approaches reaction conditions.

# 3.2. FTIR Measurements of CO on $\gamma$ -Al<sub>2</sub>O<sub>3</sub>-Supported Atomically Dispersed Rh. The CO stretching bands

characteristic of the symmetric and asymmetric frequencies of Rh(CO)<sub>2</sub> species at 2094 and 2020 cm<sup>-1</sup> are observed in CO probe molecule FTIR measurements in Ar at 298 K, after a 0.1 wt % Rh/ $\gamma$ -Al<sub>2</sub>O<sub>3</sub> catalyst was pretreated in situ for 0.5 h at 623 K in pure O<sub>2</sub> at 1 bar, followed by 10 kPa H<sub>2</sub>/Ar at 373 K for 1 h and saturated by flowing 1% CO/Ar at 1 bar for 0.5 h at 298 K (Figure 4a). The absence of CO bands in experimental FTIR spectra at frequencies characteristic of linear (~2080-2040 cm<sup>-1</sup>) and bridge- or threefold bound (~1950-1850 cm<sup>-1</sup>) CO\* on Rh clusters confirms that Rh exists primarily as atomically dispersed species following CO exposure in this sample. Tr,89 Both the symmetric and asymmetric Rh(CO)<sub>2</sub> vibrational bands are broad and non-symmetric (>20 cm<sup>-1</sup> fwhm), suggesting the presence of multiple Rh(CO)<sub>2</sub> coordination environments. 11,90,91 TPD of CO from the 0.1 wt % Rh catalyst proceeds nonuniformly across both the symmetric and asymmetric Rh(CO)<sub>2</sub> bands, as the peak centers shift to lower frequency within each band. This suggests that there are distinct  $Rh(CO)_2$  species on the  $\gamma$ -Al<sub>2</sub>O<sub>3</sub>, each with its own set of symmetric and asymmetric Rh(CO)<sub>2</sub> frequencies. Deconvolution of the FTIR spectra yields good fits to the data by including two pairs of peaks at 2094/2020 and 2084/2010 cm<sup>-1</sup> (Figure 4b). As the temperature increases from 293 to 493 K, the bands at 2094 and 2020 cm<sup>-1</sup> decrease in intensity together, while the bands at 2084 and 2010 cm<sup>-1</sup> grow, suggesting that both species are Rh(CO)<sub>2</sub> and that the first species converts to the second species as temperature increases (Table 2). At 493 K, the 2084

Table 2. Vibrational Frequencies and fwhm Parameters for Deconvoluted FTIR Stretches Associated with CO Bound to Atomically Dispersed  $Rh_1/\gamma$ - $Al_2O_3$ 

species	temperature range/K <sup>a</sup>	wavenumber/cm <sup>-1</sup>	$fwhm/cm^{-1}$
$Rh(CO)_2$	293-493 K	2094/2020	11/12
	493-603 K	2084/2010	22/29
Rh(CO)	>603 K	1985 and 1975	49 and 36

<sup>a</sup>The temperature range at which the species dominates the surface based on IR bands.

and 2010 cm<sup>-1</sup> peaks reach maximum area before decreasing. The peak positions and widths of the 2084 and 2010 cm<sup>-1</sup>

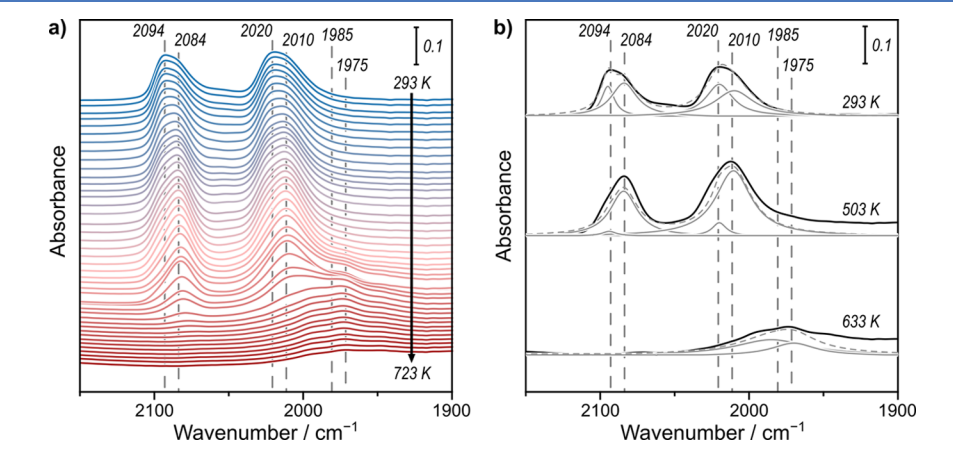
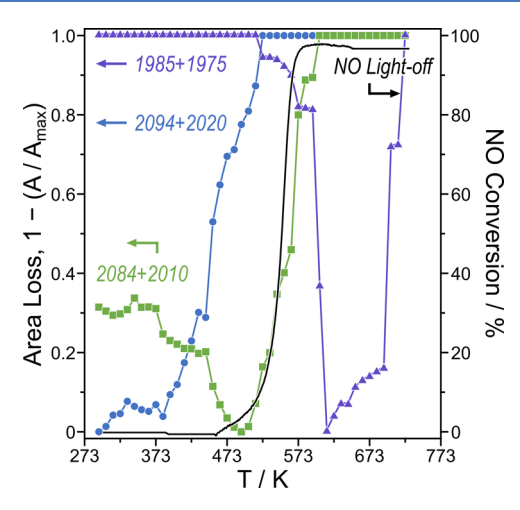


Figure 4. (a) IR spectra taken of 0.1 wt % Rh/ $\gamma$ -Al<sub>2</sub>O<sub>3</sub> every 10 K after the sample is fully saturated with CO, and as temperature increases at a rate of 0.33 K s<sup>-1</sup> (20 K min<sup>-1</sup>) from 293 K (blue) to 723 K (red). (b) Deconvolution spectra from (a) at 293, 503, and 633 K. Deconvoluted peaks (solid gray lines) are shown at each noted wavelength (2094, 2084, 2020, 2010, 1985, and 1975 cm<sup>-1</sup>) with their sum (dashed gray lines) at each temperature.

features were identified following complete loss of the 2094/ 2020 cm<sup>-1</sup> features, to enable deconvolution of the Rh(CO)<sub>2</sub> peaks in each spectrum during the TPD. The loss of 2084 and 2010 cm<sup>-1</sup> peaks occurs concurrently with the emergence and growth of bands at ~1975-1985 cm<sup>-1</sup>, which reach a maximum area at 603 K. Previous work on Rh<sub>1</sub>/TiO<sub>2</sub> suggests that these bands appear because CO desorbs sequentially from Rh(CO)<sub>2</sub> to form an Rh(CO) intermediate when the Rh is complexed to an OH species on the support. 20,83,84 Consistent with this finding, we observe that CO desorbs sequentially from Rh<sub>1</sub>/γ-Al<sub>2</sub>O<sub>3</sub>; after the first CO desorbs, a Rh(CO) species remains with CO vibrational stretches of 1975-1985 cm<sup>-1</sup>. The most prominent Rh(CO) peaks appear at 1985 and 1975 as distinct species; however, the large fwhm of these peaks (39 and 45 cm<sup>-1</sup>, respectively) indicate that the local environment around Rh(CO) varies.

The new CO vibrational frequency that appears at 1975-1985 cm<sup>-1</sup> does not coincide with the growth of any additional CO vibrational frequencies expected for terminal and bridging vibrational modes on small clusters, such as  $Rh_2(CO)_3$ ,  $^{92}$   $Rh_4(CO)_{12}$ ,  $^{93}$  or  $Rh_6(CO)_{16}$ . Furthermore, larger Rh nanoparticles, such as those formed on 10 wt % Rh/ $\gamma$ -Al<sub>2</sub>O<sub>3</sub> that we studied in our prior work," would have a bridge-bound CO\* mode far below this frequency at ~1870 cm<sup>-1</sup> and a linearly bound CO\* stretch that shifts from 2067 cm<sup>-1</sup> at high CO coverage to 1989 cm<sup>-1</sup> at the lowest observed coverage. The latter frequency is above the observed frequencies at 1985 and 1975 cm<sup>-1</sup>, which suggests that they are likely not attributable to CO\* linearly bound to Rh nanoparticles. In situ X-ray absorption spectroscopy (XAS) on the same material showed a significant increase in the Rh oxidation state and Rh-O coordination with minimal Rh-Rh coordination following the same TPD procedure.94 These XAS data indicate that Rh oxidizes rather than sinters during thermal CO desorption. Additionally, we characterized the final Rh structure here by cooling to 143 K and re-exposing the catalyst to CO to probe the final Rh structure following TPD and mitigate Rh dispersion commonly caused by CO.95 Rh(CO)<sub>2</sub> intensity increased after this CO exposure, indicating that atomically dispersed Rh species remain after TPD, but the original intensity was not fully recovered (Figure S4, Supporting Information). Rh that became oxidized after CO desorption likely would not bind CO at this temperature. No new features of linearly or bridge-bound CO were detected; therefore, metallic Rh clusters did not form or formed in an undetectably small amount. The intensity of the 1975–1985 cm<sup>-1</sup> feature also decreased following CO exposure, likely because Rh(CO)<sub>2</sub> formed from Rh(CO). As such, we assign the 1975-1985 cm<sup>-1</sup> feature to an atomically dispersed Rh monocarbonyl, Rh(CO), formed from the sequential desorption of CO molecules from  $Rh(CO)_2$ .

Interestingly, the disappearance of peaks at 2084 and 2010 cm<sup>-1</sup> closely corresponds to light-off of NO reduction by CO over atomically dispersed Rh sites (Figure 5). The coincidence of CO desorption with reactivity light-off suggests that NO–CO reactions on Rh(CO)<sub>2</sub> sites begin with the desorption of CO and that this CO desorption is a kinetically relevant step of the NO–CO reaction. This is in direct contrast to NO reduction over Rh nanoparticles, where the Rh particle surface is NO\* saturated and NO\* is consumed by dissociating during light-off (10 wt % Rh/ $\gamma$ -Al<sub>2</sub>O<sub>3</sub>, 273–673 K, 0.5 kPa CO and 0.1 kPa NO). <sup>21,77</sup> These data also indicate that NO\* reacts rapidly once CO\* is displaced from Rh<sub>1</sub>/ $\gamma$ -Al<sub>2</sub>O<sub>3</sub>. As such,



**Figure 5.** Total peak area loss for the sum of peak areas associated with the 2094 and 2020 cm<sup>-1</sup> peaks (blue, ●), 2084 and 2010 cm<sup>-1</sup> peaks (green, ■), and 1985 and 1975 cm<sup>-1</sup> peaks (purple, ▲) normalized by the maximum sum of absorbance ( $A_{\rm max}$ ) as a function of temperature during TPD overlaid with NO conversion (%, black line) as a function of temperature at a ramp rate of 0.083 K s<sup>-1</sup> in 0.5 kPa of CO and 0.1 kPa of NO over 200 mg of diluted 0.1% Rh/ $\gamma$ -Al<sub>2</sub>O<sub>3</sub> catalyst (0.2 mg Rh).

even if NO were to bind more strongly than CO—as RPBE binding energies would suggest (Figure 3)—NO\* is not stable on  $Rh_1$  at relevant reaction temperatures and is quickly consumed. This kinetic behavior also indicates the importance of the stability of adsorbates on the observed MASI: even if one species binds more strongly than another, its presence on the surface may be brief if it reacts rapidly. This result highlights the first distinct mechanistic feature of NO reduction by CO on Rh nanoparticles and  $Rh_1$ : the MASI on each active site structure differs.

The activation energy of desorption for each CO on  $\mathrm{Rh}_1$  in the experimental system can be estimated using Redhead analysis based on the temperature of the maximum desorption rate (Table 3). The 2094/2020 cm<sup>-1</sup> peaks associated with

Table 3. Desorption Energy and Enthalpy ( $\Delta H$ ) Values for CO Bound to Atomically Dispersed Rh on  $\gamma$ -Al<sub>2</sub>O<sub>3</sub>

adsorbate	peak desorption temperature, $T_{ m P}/{ m K}$	desorption energy, E/kJ mol <sup>-1</sup>	$rac{ ext{desorption}}{ ext{enthalpy,}} \Delta H/ ext{kJ mol}^{-1}$
CO from Rh(CO) <sub>2</sub>	573	148 <sup>b</sup> -161 <sup>a</sup>	$144^{b} - 157^{a}$
CO from Rh(CO)	703	199 <sup>b</sup>	193 <sup>b</sup>
difference		38-51	36-49

 $^a$ Upper limit of the CO binding energy calculated using preexponential factor (A) of  $6\times 10^{11}~\rm s^{-1}$  to account for the entropic barrier of desorption from Rh(CO)2.  $^b$ Lower limit and first-order single molecule desorption were calculated with a preexponential factor (A) of  $10^{13}~\rm s^{-1}$ .

one type of Rh(CO)<sub>2</sub> species disappear at 493 K, while the 2084/2010 cm<sup>-1</sup> peaks grow, indicating that the 2094/2020 cm<sup>-1</sup> species reconstructs to form the second species rather than desorbing. Therefore, the CO desorption energy for the 2094/2020 cm<sup>-1</sup> Rh(CO)<sub>2</sub> species cannot be computed from the TPD. Furthermore, our prior work found that the desorption of CO from Rh(CO)<sub>2</sub> had an entropic barrier,

altering the appropriate rate constant for the pre-exponential factor used in Redhead analysis (see Section 2.2.2),<sup>53</sup> justifying the use of two pre-exponential factors here— $6 \times 10^{11}$  s<sup>-</sup> (yielding an upper limit for the adsorption energy) and the canonical 10<sup>13</sup> s<sup>-1</sup>—to calculate a range of possible CO binding energies from eqs 6 and 7. The 2084/2010 cm<sup>-1</sup> peaks reach maximum rate of change at 573 K, from which the desorption energy for the first CO molecule from Rh(CO)<sub>2</sub> can be estimated as 148-161 kJ mol<sup>-1</sup>, varying with the different possible pre-exponential factors. The peaks associated with Rh(CO) species at 1985 cm<sup>-1</sup> and 1975 cm<sup>-1</sup> grow as the 2084/2010 cm<sup>-1</sup> peaks disappear, then reach their maximum rate of desorption at 703 K, yielding a desorption energy of 199 kJ mol<sup>-1</sup> for the second CO. Additionally, previous measurements for CO desorption from Rh(CO)<sub>2</sub> on a different Al<sub>2</sub>O<sub>3</sub> sample, which was reduced by CO rather than H2, showed simultaneous desorption of both CO species without Rh(CO) formation.<sup>53</sup> This suggests that the nature of the support (and likely the concentration of bound OH\* or  $H_2O^*$ ) is critical for stabilizing Rh(CO).

The Rh(CO)<sub>2</sub> with CO frequencies at 2084 and 2010 cm<sup>-1</sup> is the presumptive Rh<sub>1</sub> site from which CO desorbs to catalyze NO–CO reactions based on the comparison between in situ NO/CO reactivity during a temperature ramp and probe molecule CO TPD FTIR spectroscopy. The experimentally observed CO frequencies and CO desorption energies described here can be compared with DFT calculations of Rh(CO)<sub>2</sub> in a wide variety of environments to find a suitable model. We use this reconstruction and resulting frequency shift from 2094/2020 cm<sup>-1</sup> to 2084/2010 cm<sup>-1</sup> to further clarify the structure and local environment of the Rh(CO)<sub>2</sub> at 2084 and 2010 cm<sup>-1</sup>, which is the species most relevant to NO reduction.

**3.3. Preferred**  $\gamma$ -Al<sub>2</sub>O<sub>3</sub> **Surfaces and Model Considerations.** There are many factors that could influence the behavior of supported Rh<sub>1</sub> active sites, including the structure of the  $\gamma$ -Al<sub>2</sub>O<sub>3</sub> support, the surface facet to which the Rh<sub>1</sub> is bound, the presence of chemisorbed species that may alter the Rh<sub>1</sub> oxidation state, and the coverage of surface hydroxyl groups on the support. The high mobility of Rh(CO)<sub>2</sub> species on  $\gamma$ -Al<sub>2</sub>O<sub>3</sub> makes this range of environments available to Rh during catalysis, so we vary many of these factors to determine their effect on the adsorption and vibrational frequencies of CO\* bound to Rh<sub>1</sub>.

The bulk  $\gamma$ -Al<sub>2</sub>O<sub>3</sub> structure is typically considered a cubic defect spinel with spacegroup Fd3m;  $^{70,96-98}$  however, the precise crystal structure—particularly the location of defects within the spinel model—remains undetermined. 99,100 The surfaces of the cubic defect spinel model studied here restructure during optimization (Figure S1, Supporting Information). Recently, reconstruction of prevailing  $\gamma$ -Al<sub>2</sub>O<sub>3</sub>(110)<sub>cds</sub> facets has been detected using high-resolution transmission electron microscopy when γ-Al<sub>2</sub>O<sub>3</sub> is heated above 673 K for 1 h or more and particularly above 773  $K.^{99,101}$   $\gamma$ - $Al_2O_3$  is often formed from the dehydration of boehmite ( $\gamma$ -AlOOH) during calcination, which can leave lingering hydroxyl groups on the surface that stabilize  $\gamma$ -Al<sub>2</sub>O<sub>3</sub>(110)<sub>cds</sub> facets.  $^{35,38,39,99}$  Heating  $\gamma$ -Al<sub>2</sub>O<sub>3</sub> samples above 773 K drives off any remaining OH groups as H<sub>2</sub>O, which causes the surfaces to restructure to  $(100)_{cds}$  and  $(111)_{cds}$ facets, which are more stable without any remaining OH groups than the  $(110)_{cds}$  facets. Critically, none of the samples in this work were exposed to such high temperatures for

extended periods, suggesting that some lingering OH groups should remain on the  $\gamma$ -Al<sub>2</sub>O<sub>3</sub> surfaces and that (110)<sub>cds</sub> surfaces may still dominate.

Because of the instability of cubic defect spinel  $\gamma$ -Al<sub>2</sub>O<sub>3</sub> structures, another  $\gamma$ -Al<sub>2</sub>O<sub>3</sub> model based on the dehydration of boehmite was developed.<sup>37</sup> This structure has slightly different surfaces from the original cubic defect spinel, as emphasized in Figure 1, and does not match the  $Fd\overline{3}m$  spacegroup, but its behavior is consistent with experimental observations. 35,36 Furthermore, this structure is more stable [by 5 kJ mol-1  $(Al_2O_3 \text{ unit})^{-1}$ ] than the cubic defect spinel structure. Because this boehmite-derived model is more stable by our DFT methods and has been used and validated by many DFT studies, 35,36 we use this model in our study of supported Rh1 instead of a defect spinel model, although we acknowledge that the low crystallinity of  $\gamma$ -Al<sub>2</sub>O<sub>3</sub> may require a more precise model for specific cases. However, our goal is to develop a model that is guided by experimental observations and that is useful for future mechanistic studies of Rh<sub>1</sub>/ $\gamma$ -Al<sub>2</sub>O<sub>3</sub> catalysts, similar to earlier work on  $\gamma$ -Al<sub>2</sub>O<sub>3</sub> models themselves.

Rh atoms can bind to many different facets of the  $\gamma$ -Al<sub>2</sub>O<sub>3</sub> support. As described in Section 2.1, the differences between these cubic defect spinel (cds) and boehmite-derived (b) structures cause their Miller indices to be distinct: the (100)<sub>cds</sub> surface of the cubic defect spinel is similar to the (001)<sub>b</sub> surface of the boehmite-derived structure, and the (110)<sub>cds</sub> surface is similar to both the (100)<sub>b</sub> and (010)<sub>b</sub> surfaces of the boehmite-derived structure. Experimental X-ray diffraction studies show that the  $(110)_{cds}$  and  $(100)_{cds}$  facets dominate  $\gamma$ -Al<sub>2</sub>O<sub>3</sub> supports of various provenances, 31,98,102 so we focus our analysis of supported Rh atoms on the three similar boehmite-derived surfaces  $[(010)_b, (100)_b, and (001)_b]$ . While Rh has been shown to occupy vacancies on the surfaces of reducible oxide supports, such as  $TiO_2$ , <sup>19</sup>  $\gamma$ -Al<sub>2</sub>O<sub>3</sub> is irreducible and thus should have no or few such vacancies. Therefore, we exclude Rh structures situated in vacancies of the γ-Al<sub>2</sub>O<sub>3</sub> support from consideration. Surface formation energies for the dehydrated (100)<sub>b</sub> and (010)<sub>b</sub> surfaces are 13.2 and 12.2 kJ  $\text{mol}^{-1} \text{ Å}^{-2}$ , both higher than that for the  $(001)_b$  facet (7.3 kJ) $\text{mol}^{-1} \text{ Å}^{-2}$ ). While this indicates that the  $(001)_b$  surface is more stable than the  $(100)_b$  or  $(010)_b$  surfaces, prior work has shown that these  $(010)_b$  and  $(100)_b$  surfaces remain hydroxylated up to temperatures >700 K.  $^{35,36,38,39}$ 

**3.4. DFT Calculations of Rh(CO)**<sub>2</sub> on  $\gamma$ -Al<sub>2</sub>O<sub>3</sub>. Prior work has suggested that Rh<sub>1</sub> species in Rh(CO)<sub>2</sub> on  $\gamma$ -Al<sub>2</sub>O<sub>3</sub> occupy a +1 oxidation state based on the agreement between in situ IR studies of Rh(CO)<sub>2</sub>/γ-Al<sub>2</sub>O<sub>3</sub> and homogeneous Rh<sub>2</sub>Cl<sub>2</sub>(CO)<sub>4</sub> complexes; 12,13 however, the precise structure, vibrational modes, and charge of this species could change depending on conditions. Surface ligands derived from H<sub>2</sub>O—which can be present on the surface from boehmite dehydration, deposited during catalyst pre-treatment in air and H2, or formed from H<sub>2</sub>O in typical TWC conditions—can alter observed frequencies and binding energies. Therefore, we consider a range of  $O_x H_v^*$  (x = 0-1, y = 0-1) ligands attached to Rh<sub>1</sub> to alter the oxidation state and coordination of the Rh<sub>1</sub> species to the surface of  $\gamma$ -Al<sub>2</sub>O<sub>3</sub>. No calculations in this work were run with a net charge; instead, the ligand attached to Rh<sub>1</sub> sets its oxidation state. For example, an O\* has an oxidation state of -2, forcing the Rh<sub>1</sub> into an oxidation state of +2, while an  $OH^*$  has a net oxidation state of -1, forcing the  $Rh_1$  into a +1oxidation state.

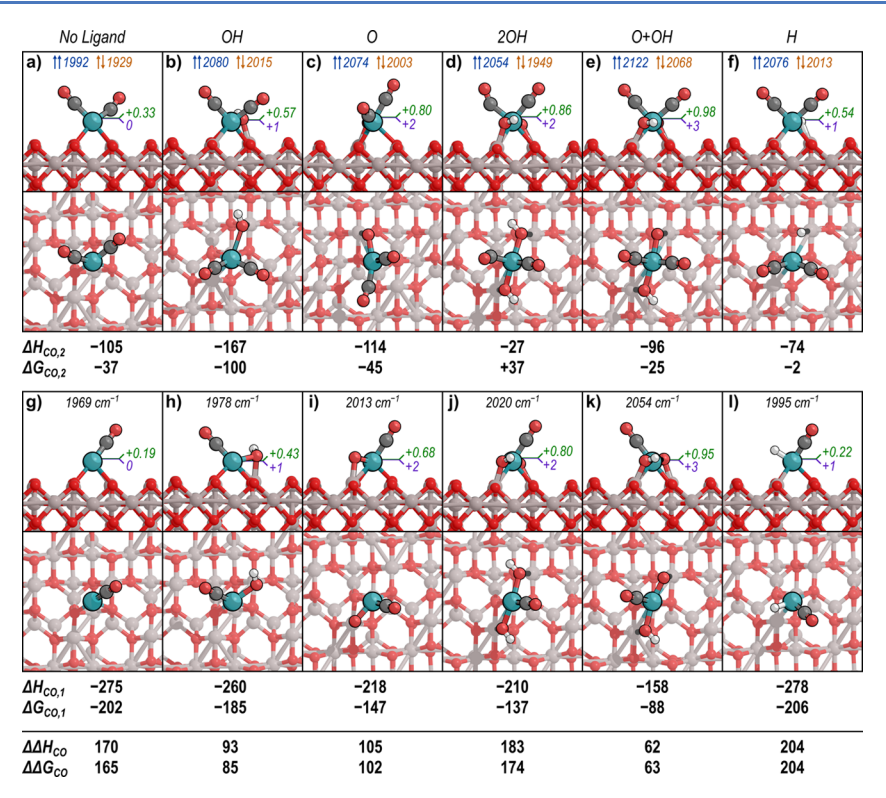


**Figure 6.** Models of (a–f) Rh<sub>1</sub>(CO)<sub>2</sub> and (g–l) Rh<sub>1</sub>(CO) on  $\gamma$ -Al<sub>2</sub>O<sub>3</sub>(010)<sub>b</sub> [corresponding to the (110)<sub>cds</sub> surface of spinel defect  $\gamma$ -Al<sub>2</sub>O<sub>3</sub> shown parallel to (top) and perpendicular to (bottom) the  $\gamma$ -Al<sub>2</sub>O<sub>3</sub> surface. The Rh<sub>1</sub> is shown with different co-adsorbed species in each column: (a,g) Rh(0) with no ligands, (b,h) Rh(I) with an OH ligand, (c,i) Rh(II) with an O ligand, (d,j) Rh(II) with two OH ligands, (e,k) Rh(III) with O and OH ligands, and (f,l) Rh(I) with an H ligand. CO\* vibrational frequencies are shown above each structure in cm<sup>-1</sup>, including symmetric (blue, ↑↑) and asymmetric (orange, ↑↓) stretches above the Rh(CO)<sub>2</sub> species. Calculated binding enthalpies ( $\Delta H_{CO}$ ) and free energies ( $\Delta G_{CO}$ ) at 473 K are shown below their corresponding structures. The Rh oxidation state and estimated partial charges from QUAMBO are shown for each structure in purple and green, respectively. The difference in the binding enthalpy ( $\Delta \Delta H_{CO}$ ) and free energy ( $\Delta \Delta G_{CO}$ ) between the first and second CO\* is shown beneath each set of structures in kJ mol<sup>-1</sup>. Additional images are shown in Figures S13 and S14 of the Supporting Information.

We begin by analyzing models with  $Rh_1$  on the  $(010)_b$  surface of the boehmite-derived model, which is similar to the most abundant  $\gamma$ - $Rl_2O_3(110)_{cds}$  facet and has a lower surface formation energy than the  $(100)_b$  surface. While previous work has shown the macroscopic  $(110)_{cds}$  facet to be comprised of nanosized  $(111)_{cds}$  and  $(100)_{cds}$  facets on some forms of  $\gamma$ - $Rl_2O_3$ , we still consider the  $(010)_b$  facet [equivalent to the  $(110)_{cds}$  facet] to develop a DFT model suitable for examining the effects of Rh oxidation state, types of Rh ligands, and local hydroxyl concentration on  $Rh(CO)_2$  desorption behavior. We validate this model with FTIR spectroscopy of  $Rh(CO)_2$  in commercially available  $\gamma$ - $Rl_2O_3$  found in catalytic converters to capture behavior relevant to  $NO_x$  reduction.

To minimize the complexity of the DFT model, we begin these studies absent hydroxyls on the  $\gamma$ -Al<sub>2</sub>O<sub>3</sub> surface, apart from those coordinated to Rh<sub>1</sub>, and examine the role of surface hydroxyls in Section 3.5. The structures of the most stable Rh(CO) and Rh(CO)<sub>2</sub> analyzed in this work with different ligands on otherwise de-hydroxylated  $\gamma$ -Al<sub>2</sub>O<sub>3</sub>(010)<sub>b</sub> are shown in Figure 6. Partial charges estimated by QUAMBO<sup>69</sup> indicate that, despite ostensibly having an oxidation state of 0, Rh<sub>1</sub> carries partial charge of +0.33 e in the Rh(CO)<sub>2</sub> structure without any ligands, with this charge balanced by the  $\gamma$ -Al<sub>2</sub>O<sub>3</sub> support (-0.18 e) and CO ligands (-0.15 e). As various O\* and OH\* ligands are added, the formal charge assigned to Rh<sub>1</sub> increases up to +3, and the computed partial charges increase linearly up to +0.98, as shown in Figure 7, presenting a strong correlation between the formal charge assignments and the

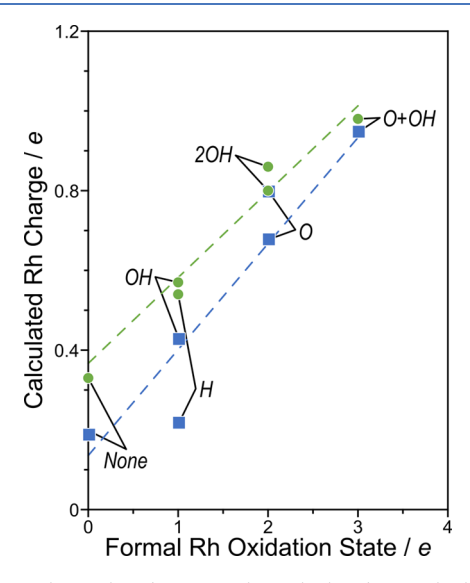


**Figure** 7. Relationship between the calculated partial charge and formal oxidation state of the Rh single atom on  $\gamma$ -Al<sub>2</sub>O<sub>3</sub> as an Rh(CO) ( $\blacksquare$ , blue) and Rh(CO)<sub>2</sub> ( $\bullet$ , green) with a variety of ligands attached. Each point is labeled with its corresponding ligand(s). Dashed lines are to guide the eye.

partial charges obtained by QUAMBO. Additionally, partial charge estimates of the  $Rh_1$  in  $Rh(CO)_2$  appear to be systematically higher than those in Rh(CO) across all ligands tested in this work. These higher charges on the  $Rh_1$  in

Table 4. Summary of the Characteristics from Experimental Observations of CO\* on a 0.1 wt %  $Rh/\gamma$ - $Al_2O_3$  Sample and the DFT-Studied Model That Most Closely Matches Those Observations on the  $(010)_b$  Surface without Nearby OH\* Groups Derived from  $H_2O$  on the Support

species	$Rh(CO)_2$ frequencies/cm <sup>-1</sup>	Rh(CO) frequency/cm <sup>-1</sup>	$\Delta \Delta H_{\rm CO}/{\rm kJ~mol^{-1}}$
experiment	2094/2020 and 2084/2010	1975 and 1985	36-49
$HO-Rh^{+1}$ (DFT)	2080/2015	1978	93

 $Rh(CO)_2$  indicate that the additional CO\* helps to stabilize a more ionic Rh center by accepting some electrons, despite CO being formally neutral. This correlation without exact quantitative agreement between calculated partial charges and formal oxidation states corroborates prior work that has shown that computed partial charges do not quantitatively match formal oxidation state assignments in bulk materials. Notably, adding H\* to the Rh<sub>1</sub> results in an increase in the partial charge on Rh<sub>1</sub>, suggesting that it behaves as a hydride rather than as a proton when bound to these  $Rh(CO)_x$  species. As such, the charge on the Rh<sub>1</sub> in  $H-Rh(CO)_x$  is similar to the partial charges on Rh<sub>1</sub> in  $HO-Rh(CO)_x$  supporting a +1 formal charge assignment for this species (Figures 6f and 6l).

On the dehydrated (010)<sub>b</sub> surface, the binding enthalpy  $(\Delta H_{\rm CO,2})$  and free energy  $(\Delta G_{\rm CO,2})$  of CO\* to form Rh(CO)<sub>2</sub> from Rh(CO) with no additional ligands on Rh are -105 and -37 kJ mol<sup>-1</sup> respectively, as shown in Figure 6a. The adsorption free energy is less negative than the enthalpy because of a 106 J mol<sup>-1</sup> K<sup>-1</sup> entropy loss of CO upon adsorption. The binding enthalpies for the second CO\* [to form Rh(CO)<sub>2</sub> from Rh(CO)] vary from -167 to -27 kJ mol<sup>-1</sup> when additional ligands are present on the Rh<sub>1</sub> (Figure 6a-f), indicating that these ligands can either make Rh<sub>1</sub> bind CO\* more (e.g., OH ligand) or less (e.g., H ligand) strongly, with similar trends seen for the binding free energies. Critically, the partial charge on the Rh<sub>1</sub> does not predict CO\* binding energies, as the partial charges on Rh<sub>1</sub> in Rh(CO)<sub>2</sub> in the presence of OH\* and H\* ligands are nearly identical (+0.57 and +0.54, respectively), while the CO\* binding enthalpies are very different (-167 and -74 kJ mol<sup>-1</sup>). Adding a second O\* or OH\* ligand results in significantly weaker CO\* binding energies (Figure 6d,e). In each case where there is an additional ligand bound to the Rh<sub>1</sub> (O, OH, or H), the remaining CO\* prefers to be oriented away from the ligand. These data show that the Rh<sub>1</sub> oxidation state and the presence of charge-altering Rh<sub>1</sub> ligands significantly change the adsorption energies of CO\* in Rh(CO)<sub>2</sub> complexes.

The CO\* in the monocarbonyl, Rh(CO), binds much more strongly than the first CO\* when no ligand is present, with  $\Delta H_{\rm CO,1}$  of -275 kJ mol<sup>-1</sup> compared to  $\Delta H_{\rm CO,2}$  of -105 kJ mol<sup>-1</sup> for the second CO\* to form Rh(CO)<sub>2</sub> from Rh(CO). The binding energies of CO\* in Rh(CO) ( $\Delta H_{\text{CO},1}$  and  $\Delta G_{CO,1}$ ) are generally less exothermic with added  $O_rH_r$ ligands, except for the H ligand, which slightly strengthens the CO\* binding energy. These data suggest that strong coadsorbate interactions between the CO\* in Rh(CO)2 weaken the binding of the second CO\* relative to the first. The result of this interaction, in turn, suggests that CO would desorb from Rh(CO), sequentially through a monocarbonyl intermediate when additional ligands are coordinated to Rh<sub>1</sub>. This sequential desorption process is in qualitative agreement with FTIR-TPD data (Figure 4 and Section 3.1). The adsorption energies calculated here, particularly for the second CO\*, are near those estimated by Redhead analysis of the TPD data

collected in this work (Table 3). While the absolute values for these adsorption energies are difficult to accurately determine from experiment, their differences ( $\Delta\Delta G_{\rm CO}$  and  $\Delta\Delta H_{\rm CO}$ ) are instructive: CO\* desorption from Rh(CO)<sub>2</sub> has a Redheadestimated binding energy from experimental data that is ~50 kJ mol<sup>-1</sup> weaker than for CO\* desorption from Rh(CO), while the  $\Delta\Delta H_{\rm CO}$  estimated from DFT ranges from 62 kJ mol<sup>-1</sup> [for Rh<sup>3+</sup>(CO)<sub>2</sub> with O and OH ligands] to 170 kJ mol<sup>-1</sup> [for  $Rh^{0}(CO)_{2}$  without additional ligands]. For the  $Rh^{+}(CO)_{2}$  with an OH ligand, the model embraced by prior work on TiO<sub>2</sub>, <sup>20</sup> the  $\Delta\Delta H_{\rm CO}$  is 93 kJ mol<sup>-1</sup>, larger than the 50 kJ mol<sup>-1</sup> suggested by Redhead estimates (Table 3). These discrepancies likely arise from the instability of the "bare" Rh atom that would result from CO\* desorption from Rh(CO) in the calculations. This bare Rh<sub>1</sub> would reconstruct upon the second CO\* desorption to coordinate with species native to the support and may also change its oxidation state—details absent from the current DFT study and unobservable from FTIR studies. The vibrational frequency data from the FTIR, furthermore, provides a reliable characterization against which these DFT models can be compared.

While CO\* binding energies can either increase or decrease upon the addition of these ligands to Rh<sub>1</sub>, the vibrational frequencies always increase relative to the structure without additional ligands (Figure 6). The symmetric and asymmetric stretches of Rh(CO)<sub>2</sub> increase by 60-130 and 20-138 cm<sup>-1</sup>, respectively, and the single CO\* stretch frequency for the Rh(CO) increases by 8-85 cm<sup>-1</sup> upon ligand addition (Figure 6). An O2- ligand (O), a combination of two OH- ligands (2OH), and a combination of O<sup>2-</sup> and OH<sup>-</sup> ligands (O + OH) place  $Rh_1$  into +2, +2, and +3 oxidation states, respectively. These states do not match with prior XPS and FTIR studies of Rh<sub>1</sub>/ $\gamma$ -Al<sub>2</sub>O<sub>3</sub> that indicated that Rh is in a +1 oxidation state. 11-13 Our data confirm these results: calculated stretching frequencies for the Rh(CO)<sub>2</sub> species with these ligands generally differ by >10 cm<sup>-1</sup> from those observed experimentally (Table 2). When H is coordinated to Rh<sub>1</sub>, the symmetric and asymmetric stretching frequencies for the gemdicarbonyl structure (2076 and 2013 cm<sup>-1</sup>) are similar to those from IR spectra ( $\sim 2090/\sim 2015$  cm<sup>-1</sup>), but the binding enthalpies (-278 and -74 kJ mol<sup>-1</sup>) disagree with experimental values (-193 and -150 kJ mol<sup>-1</sup>). When an OH ligand is present, the symmetric and asymmetric stretching frequencies for Rh(CO)<sub>2</sub> (2080 and 2015 cm<sup>-1</sup>, respectively) are in close agreement to the second set of frequencies observed during IR TPD (2084 and 2010 cm<sup>-1</sup>). These data suggest that the presence of ligands can alter the Rh<sub>1</sub> oxidation state, CO\* adsorption energies, and CO\* stretch frequencies. Furthermore, these data suggest that the Rh(CO)<sub>2</sub> species observed during both in situ FTIR and CO probe molecule FTIR experiments is most likely coordinated to OH-, as summarized in Table 4, consistent with prior work examining Rh single atoms on other oxide supports, such as TiO<sub>2</sub><sup>19,20,</sup> and ZrO<sub>2</sub>.84

We now turn to other facets of  $\gamma$ -Al<sub>2</sub>O<sub>3</sub> also prevalent on  $\gamma$ -Al<sub>2</sub>O<sub>3</sub> supports:  $(100)_b$ —which, like  $(010)_b$ , resembles  $(110)_{cds}$ —and  $(001)_b$ , which resembles  $(100)_{cds}$ . Rh<sub>1</sub> may behave differently on these other facets; for example, 0.5 wt % Rh/CeO<sub>2</sub> samples contain three different sets of peaks that may correspond to Rh<sub>1</sub> on different facets with different activities for NO reduction. The most stable termination of the  $(001)_b$  surface has Al sites that are all fivefold coordinated and therefore have lower Lewis acid strength than the Al of the  $(100)_b$  and  $(010)_b$  surfaces of Al. Reanwhile, the most stable  $(100)_b$  surface, after optimization, has a threefold coordinated Al site, which is a stronger Lewis acid than other fourfold coordinated Al on the  $(100)_b$  and  $(010)_b$  surfaces. Again, for simplicity, we begin by examining  $\gamma$ -Al<sub>2</sub>O<sub>3</sub> surfaces absent hydroxyls apart from an OH ligand directly bound to Rh.

CO binding strengths to  $Rh_1$  are similar when  $Rh_1$  resides on the  $(010)_b$  and  $(100)_b$  surface facets (both of which correspond to the  $(110)_{cds}$  facet of the cubic defect spinel  $\gamma$ -Al<sub>2</sub>O<sub>3</sub>), with differences of 5 and 16 kJ mol<sup>-1</sup> for the first and second CO adsorption (Figure 8). CO binding energies to  $Rh_1$  on the  $(001)_b$  surface [corresponding to the  $(100)_{cds}$  facet of the cubic defect spinel  $\gamma$ -Al<sub>2</sub>O<sub>3</sub>], however, are ~50 kJ mol<sup>-1</sup> less exothermic than those on the other facets. The differences between the first and second CO adsorption energies remain near 100 kJ mol<sup>-1</sup> across all three facets for these OH<sup>-</sup>-coordinated  $Rh^+(CO)_2$  species, with the smallest gap (in closest agreement with the Redhead analysis) observed on the  $(010)_b$  surface.

Additionally, we calculate the interaction energy between the  $Rh(CO)_2$  and each facet  $(\Delta E_{int})$ , which is the energy to bind a gas-phase  $Rh(CO)_2$  to the alumina facet with one OH group

$$Rh(CO)_{2(g)} + OH^* \rightarrow HO - Rh(CO)_2^*$$
 (8)

This interaction energy is the strongest on the  $(010)_b$  facet at -388 kJ mol<sup>-1</sup>, followed closely by the  $(100)_b$  facet (-387 kJ mol<sup>-1</sup>), both of which are much stronger than  $\Delta E_{\rm int}$  on the  $(001)_b$  surface (-334 kJ mol<sup>-1</sup>) (Figure 8). This further indicates that HO–Rh(CO)<sub>2</sub> is likely to form on  $(010)_b$  or  $(100)_b$  facets during synthesis.

The symmetric and asymmetric stretching frequencies of the  $HO-Rh(CO)_2$  species on the  $(001)_b$  and  $(100)_b$  surfaces are higher than those on the  $(010)_b$  surface by 6–14 cm<sup>-1</sup>, with larger differences for the symmetric stretch between surfaces (Figure 8). Critically, these vibrational frequencies do not directly correlate to CO\* binding energies (as also observed when we altered ligands, Figure 6). Frequencies of the HO-Rh(CO)<sub>2</sub> on each surface agree relatively well with measured values, given the range of frequencies observed in FTIR spectroscopy (2084 and 2094 cm<sup>-1</sup> for symmetric and 2010 and 2020 cm<sup>-1</sup> for asymmetric). Stretching frequencies for the HO-Rh(CO) species are also larger on the (100)<sub>b</sub> and (001)<sub>b</sub> surfaces (2007 and 2013 cm<sup>-1</sup>, respectively) than on the (010)<sub>b</sub> surface (1978 cm<sup>-1</sup>), with the latter being more similar to measured values (1975 and 1985 cm<sup>-1</sup>). This suggests that the shift in frequencies observed in the IR TPD from 2094/ 2020 to 2084/2010 cm $^{-1}$  may be explained by HO-Rh(CO)<sub>2</sub> moving from the (001)<sub>b</sub> surface (frequencies of 2093/2020 cm<sup>-1</sup>) or the  $(100)_b$  surface (frequencies of 2094/2027 cm<sup>-1</sup>) to the (010)<sub>b</sub> surface (frequencies of 2080/2015 cm<sup>-1</sup>), from which CO\* desorbs to form a monocarbonyl with a CO\* stretch frequency measured near 1980 cm<sup>-1</sup>; however, these

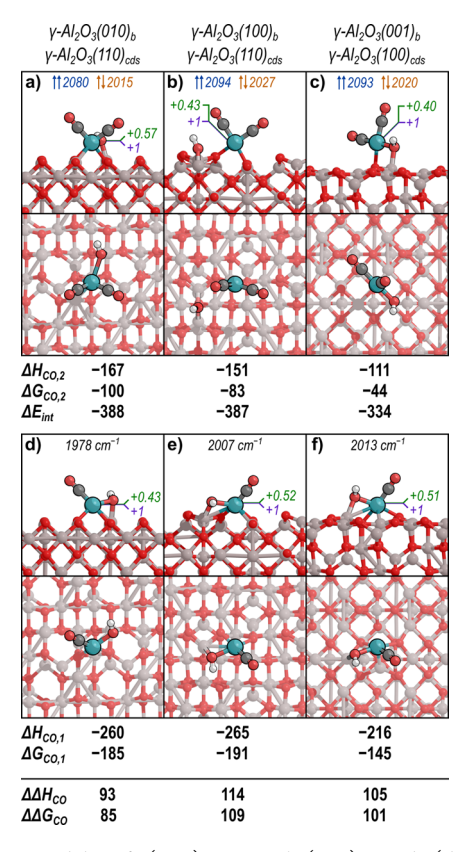


**Figure 8.** Models of (a−c) HO−Rh<sub>1</sub>(CO)<sub>2</sub> and (d−f) HO−Rh<sub>1</sub>(CO) on (a,d)  $\gamma$ -Al<sub>2</sub>O<sub>3</sub> (010)<sub>b</sub> [equivalent to  $\gamma$ -Al<sub>2</sub>O<sub>3</sub>(110)<sub>cds</sub>], (b,e)  $\gamma$ -Al<sub>2</sub>O<sub>3</sub> (100)<sub>b</sub> [equivalent to  $\gamma$ -Al<sub>2</sub>O<sub>3</sub>(110)<sub>cds</sub>], and (c,f)  $\gamma$ -Al<sub>2</sub>O<sub>3</sub>(001)<sub>b</sub> [equivalent to  $\gamma$ -Al<sub>2</sub>O<sub>3</sub>(100)<sub>cds</sub>], surfaces shown from the top and from the side. For each structure, the CO\* vibrational frequencies are shown in cm<sup>-1</sup>, including symmetric (blue, ↑↑), asymmetric (orange, ↑↓), and monocarbonyl (black) stretches where appropriate. The assigned formal Rh oxidation state (purple) and partial charges from QUAMBO analysis (green) are also shown in  $\epsilon$ . Binding enthalpies ( $\Delta H_{\rm CO}$ ) and free energies ( $\Delta G_{\rm CO}$ ) for each CO\*, the interaction energy between the Rh(CO)<sub>2</sub> and each facet ( $\Delta E_{\rm int}$ ), as well as the differences for each between the first and second CO\* ( $\Delta \Delta H_{\rm CO}$  and  $\Delta \Delta G_{\rm CO}$ ) at 473 K are shown in kJ mol<sup>-1</sup> below their corresponding structures. Additional images are shown in Figures S15 and S16 in the Supporting Information.

calculations neglect the role of OH coverage, which may also lead to the FTIR spectroscopy evolution during the TPD.

3.5. Effects of  $H_2O$  Adsorption to  $\gamma$ -Al<sub>2</sub>O<sub>3</sub> on Rh(CO)<sub>2</sub> Frequencies. Hydroxyl species (OH) likely exist at high coverages on  $\gamma$ -Al<sub>2</sub>O<sub>3</sub> surfaces formed from H<sub>2</sub>O-derived H\* and OH\* species bound to Brønsted basic O atoms or Lewis acidic Al of the support, <sup>38</sup> respectively

$$H_2O_{(bulk)} + O_s + Al_s \rightleftharpoons HO_s + HOAl_s$$
 (9)

where  $H_2O_{(bulk)}$  is  $H_2O$  in the bulk (gas or liquid phase, gas modeled here), while  $O_s$  and  $Al_s$  are atoms on the support surface. In addition to these dissociated complexes,  $H_2O$  may also adsorb molecularly

$$H_2O_{(bulk)} + * \rightleftharpoons H_2O^*$$
 (10)

The coverage of these  $H^*/OH^*$  (abbreviated herein as  $OH^*$ ) and  $H_2O^*$  can be described in terms of total (dissociated and molecular) water content ( $\theta_W$ ), in units of  $OH \ nm^{-2}$  (when  $H_2O$  adsorbs dissociatively, with 2  $OH \ per H_2O$  adsorbed) or  $H_2O \ nm^{-2}$  (when  $H_2O$  begins to adsorb

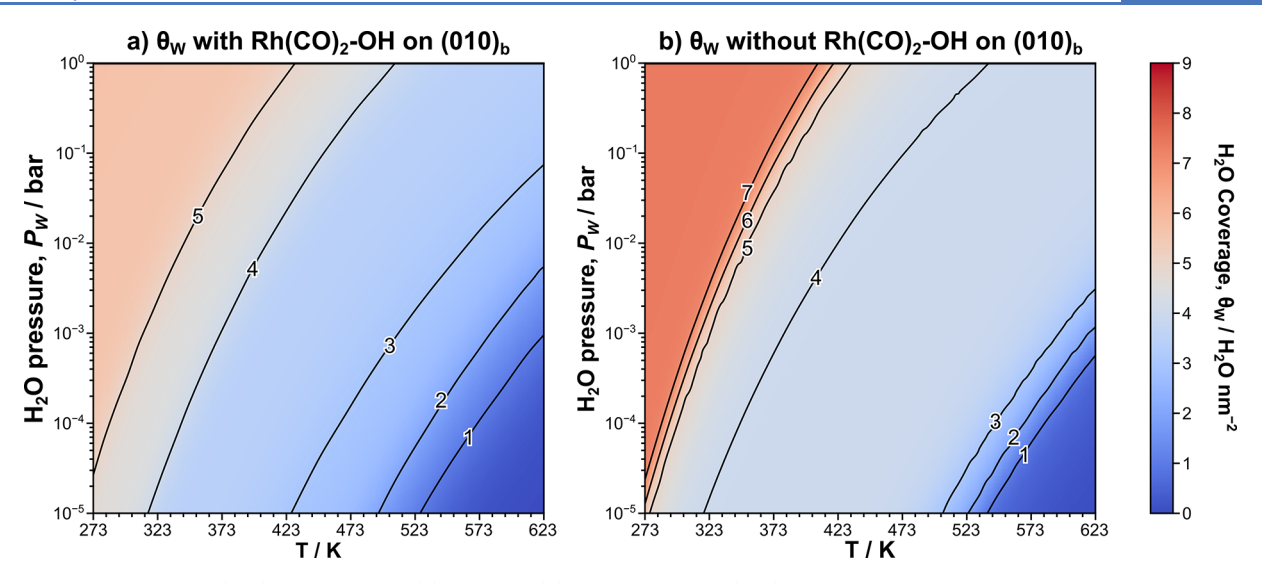


Figure 9.  $H_2O$  coverage on  $(010)_b$  surfaces both (a) with and (b) without  $HO-Rh(CO)_2$  present as a function of  $H_2O$  pressure and temperature based on equilibrium constants for dissociative or associative  $H_2O$  adsorption under standard conditions (473 K, 1 bar  $H_2O$ ). All coverages are presented in units of  $H_2O$  nm<sup>-2</sup>, although  $H_2O$  dissociatively adsorbs to form  $H^*/OH^*$  pairs below 3.96  $H_2O$  nm<sup>-2</sup> (7.92 OH nm<sup>-2</sup>) in (a) and below 4.52  $H_2O$  nm<sup>-2</sup> (9.05 OH nm<sup>-2</sup>) in (b).

molecularly). These OH\* and  $H_2O^*$  may influence the CO\* adsorption energies and/or vibrational frequency of CO\* on Rh<sub>1</sub>. As the coverages of OH\* and  $H_2O^*$  are expected to decrease with increasing temperature, understanding how these influence CO\* behavior is critical for understanding the CO FTIR TPD data and likely the species involved in the CO–NO reaction. As such, we systematically evaluate the effects of changing  $\theta_W$  on CO\* frequencies and binding energies using DFT, including coverages above which the surface saturates and where  $H_2O$  molecularly physisorbs in bilayers above the support.

We calculate  $\theta_W$  on the  $\gamma$ -Al<sub>2</sub>O<sub>3</sub> surface in a range of temperatures and water pressures to explore possible hydroxylated and hydrated environments (for details, see Section S5, Supporting Information). We also assess  $\theta_{\rm W}$  with and without a  $HO-Rh(CO)_2$  complex to determine the most stable environment around HO-Rh(CO)2, how adsorbed H<sub>2</sub>O\* affects CO\* stretch frequencies, and the extent to which Rh<sub>1</sub> species displace OH\* and H<sub>2</sub>O\* upon adsorption. Equilibrium constants for H<sub>2</sub>O adsorption were calculated on each facet tested in this work based on the sequential adsorption free energies of  $H_2O$ ,  $\Delta G_W$ , at 473 K and 1 bar  $\rm H_2O$  (standard pressure). Prior DFT studies  $^{35,38}$  indicated that the (001)<sub>b</sub> surface of this γ-Al<sub>2</sub>O<sub>3</sub> model had no OH\* above 600 K but that OH\* remained on the (100)<sub>b</sub> and (010)<sub>b</sub> surfaces up to 1100 K. Here, we also examine the coverage of dissociatively and molecularly adsorbed H<sub>2</sub>O\* on the (010)<sub>b</sub> surface and how the HO-Rh(CO)<sub>2</sub> species may influence those coverages. Then, we address the effects of  $\theta_{\mathrm{W}}$  on the behavior of this HO-Rh(CO)<sub>2</sub> species because it is the most likely candidate structure for a Rh single atom.

Calculations of OH\* and  $\rm H_2O^*$  on  $\gamma$ -Al<sub>2</sub>O<sub>3</sub>(010)<sub>b</sub> confirm previous results,  $^{38,39}$  indicating that the surfaces corresponding to  $\gamma$ -Al<sub>2</sub>O<sub>3</sub>(110)<sub>cds</sub> are partly covered with OH\* even above 500 K and with water pressures below  $10^{-4}$  bar when studied at 373–623 K and  $10^{-5}$  to  $10^0$  bar (Figure 9). We examined concentrations of 0–15.27 and 0–9.05  $\rm H_2O~mm^{-2}$  on (010)<sub>b</sub> with and without HO–Rh(CO)<sub>2</sub>, respectively, where the model has a surface area of 1.77 nm². We explored higher

coverages around HO-Rh(CO)<sub>2</sub> to determine how water solvating the Rh<sub>1</sub> altered the vibrational frequencies of the bound CO\*. Notably, there are 8 exposed Al atoms on this  $\gamma$ -Al<sub>2</sub>O<sub>3</sub>(010)<sub>b</sub> model, and H<sub>2</sub>O prefers to adsorb dissociatively until each Al atom is covered. When there is no HO- $Rh(CO)_2$  present, this saturation occurs with 8  $H_2O$  molecules at a coverage of 9.05 OH nm<sup>-2</sup> (NB: each adsorbed H<sub>2</sub>O\* produces two OH\* species in these units of coverage). When HO-Rh(CO)<sub>2</sub> is present, its OH occupies one Al and H<sub>2</sub>O stops adsorbing dissociatively at 7.92 OH nm<sup>-2</sup>, not counting the OH attached to the  $Rh_1$ . The  $\Delta G_w$  values remain negative-indicating favorable binding-up to 9.05 OH nm<sup>-2</sup> on  $\gamma$ -Al<sub>2</sub>O<sub>3</sub>(010)<sub>b</sub> when HO-Rh(CO)<sub>2</sub> is absent (473 K and 1 bar H<sub>2</sub>O, Figure S5, Supporting Information). Specifically, OH concentrations do not drop below 1.2 OH  $nm^{-2}$  on  $(010)_b$  without HO-Rh(CO)<sub>2</sub> at 623 K and  $10^{-4}$  bar H<sub>2</sub>O (presented in Figure 9 in units of total H<sub>2</sub>O nm<sup>-2</sup>) and peak at 7.35 H<sub>2</sub>O nm<sup>-2</sup> at 273 K and 1 bar (although H<sub>2</sub>O forms ice under these conditions). The H<sub>2</sub>O-derived adlayer at this maximum coverage comprises 8 dissociated H<sub>2</sub>O in the form of H\*/OH\* pairs (a coverage of 9.05 OH nm<sup>-2</sup>) and 5 molecularly adsorbed H<sub>2</sub>O (an additional coverage of 2.83 molecular H<sub>2</sub>O nm<sup>-2</sup>) (see Figures S5-S12 in the Supporting Information for images of all hydrated γ-Al<sub>2</sub>O<sub>3</sub> structures studied in this work). While water is not co-fed under most conditions in this work, trace water in the feed and residual hydroxyls from the hydrothermal synthesis and reduction of the initially oxidized Rh by H2 are expected during TPD experiments. Moreover, the conditions under which TWCs typically operate include ~10% water, which leads to support hydroxylation and water adsorption. Even trace amounts of water can lead to significant changes in catalytic behavior, perhaps best illustrated by the behavior of Au/TiO2 during CO oxidation, during which trace H2O shuttles H atoms to facilitate O<sub>2</sub> dissociation at the Au interface with TiO<sub>2</sub>. 107,108 Next, we evaluate surface hydroxylation in the presence of HO-Rh(CO)<sub>2</sub> species on  $\gamma$ -Al<sub>2</sub>O<sub>3</sub>(010)<sub>b</sub>.

When HO-Rh(CO)<sub>2</sub> is present on the  $\gamma$ -Al<sub>2</sub>O<sub>3</sub> surface, surface hydroxylation decreases (Figure 9a). The coverages are

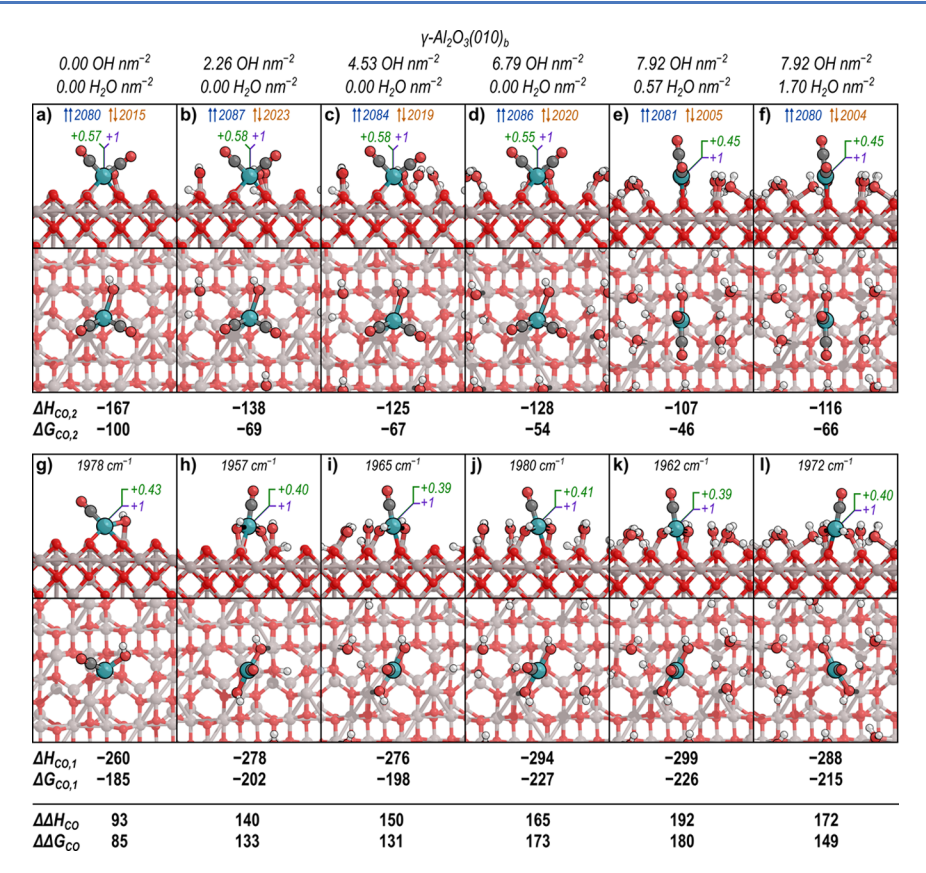


Figure 10. Models of (a-f) HO-Rh<sub>1</sub>(CO)<sub>2</sub> and (g-l) HO-Rh<sub>1</sub>(CO) on  $\gamma$ -Al<sub>2</sub>O<sub>3</sub>(010)<sub>b</sub> with adsorbed H<sub>2</sub>O coverages of (a,g) 0.0 OH nm<sup>-2</sup>, (b,h) 2.26 OH nm<sup>-2</sup>, (c,i) 4.53 OH nm<sup>-2</sup>, (d,j) 6.79 OH nm<sup>-2</sup>, (e,k) 7.92 OH nm<sup>-2</sup> and 0.57 H<sub>2</sub>O nm<sup>-2</sup> (where H<sub>2</sub>O first adsorbs molecularly), and (f,l) 7.92 OH nm<sup>-2</sup> and 1.70 H<sub>2</sub>O nm<sup>-2</sup> from additional H<sub>2</sub>O dissociated on the  $\gamma$ -Al<sub>2</sub>O<sub>3</sub> surface. For each structure, the CO\* vibrational frequencies are shown in cm<sup>-1</sup>, including symmetric (blue, ↑↑), asymmetric (orange, ↑↓), and monocarbonyl (black) stretches where appropriate. The assigned formal Rh oxidation state (purple) and partial charges from QUAMBO analysis (green) are also shown in  $\epsilon$ . Binding enthalpies ( $\Delta H_{CO}$ ) and free energies ( $\Delta G_{CO}$ ), as well as the differences for each between the first and second CO\* ( $\Delta \Delta H_{CO}$  and  $\Delta \Delta G_{CO}$ ) at 473 K, are shown in kJ mol<sup>-1</sup> below their corresponding structures. Additional views of these structures and other structures with varying OH coverages are shown in Figures S5–S10 of the Supporting Information.

 $0.05-7.35 \text{ H}_2\text{O nm}^{-2}$  without  $HO-Rh(CO)_2$  (373-623 K,  $10^{-5}-10^{0}$  bar H<sub>2</sub>O), which drops to 0.02-5.73 H<sub>2</sub>O nm<sup>-2</sup> when the  $HO-Rh(CO)_2$  is present. This decrease in coverage indicates that OH groups are locally displaced by the HO-Rh(CO)<sub>2</sub> (NB: these coverages exclude the OH group to which the Rh<sub>1</sub> is attached). Dilute Rh<sub>1</sub> on γ-Al<sub>2</sub>O<sub>3</sub> likely negligibly affects sample-averaged  $\theta_{\mathrm{W}}$ , except in their immediate vicinities. For the IR spectra that were recorded under "dry" conditions in this work, DFT predicts that hydroxyl coverages on the (010)<sub>b</sub> surface should be low if adsorption and desorption of H2O are quasi-equilibrated, although their relative density would still decrease with increasing temperature according to these data. Previous experimental studies, however, suggest that average hydroxyl coverages may be 8-12 OH nm<sup>-2</sup>, with OH distributed heterogeneously, such that some regions of  $\gamma$ -Al<sub>2</sub>O<sub>3</sub> exceed this range. 40,41

Rh(CO)<sub>2</sub> remains bound to two surface O atoms of the  $\gamma$ -Al<sub>2</sub>O<sub>3</sub> support at coverages where H<sub>2</sub>O adsorbs dissociatively ( $\leq$ 7.92 OH nm<sup>-2</sup>; Figure 10a-d). The presence of these H\*/OH\* pairs on  $\gamma$ -Al<sub>2</sub>O<sub>3</sub>(010)<sub>b</sub> weakens the binding energy for the second CO\* to form Rh(CO)<sub>2</sub> from Rh(CO), shifting  $\Delta H_{\rm CO,2}$  from -167 to -116 kJ mol<sup>-1</sup> as the surface becomes increasingly hydrated (Figure 10a-f). Hydration, however, strengthens binding for the first CO [to form Rh(CO), Figure 10] with  $\Delta H_{\rm CO,1}$  decreasing from -260 to -288 kJ mol<sup>-1</sup> over

this same range. These additional H\*/OH\* can coordinate to the Rh<sub>1</sub> without altering its oxidation state, which confers some additional stability when the Rh is bare and when only one CO\* is adsorbed but more so for the latter. When the second CO adsorbs to form Rh(CO)<sub>2</sub>, these additional OH\* both stabilize the preceding state and repel the additional CO\* on the now-saturated Rh<sub>1</sub>; as such, binding energies for the second CO\* weaken with additional OH\* on the surface. These contradicting trends cause the  $\Delta \Delta H_{\rm CO}$  to increase from 93 to 172 kJ mol<sup>-1</sup>, far above the experimentally estimated  $\Delta\Delta H_{\rm CO}$  of 36–49 kJ mol<sup>-1</sup>. However, desorption from Rh(CO) to form a "bare" Rh, as modeled here, is unlikely to occur in experiments, leading to some doubts in DFT-derived  $\Delta\Delta H_{\rm CO}$  energies. Instead, it is likely that new ligands (wateror surface-derived OH\*) take the place of desorbed CO\* on the resulting Rh<sub>1</sub>/ $\gamma$ -Al<sub>2</sub>O<sub>3</sub> species. These structural changes of the bare Rh cannot be fully described by FTIR spectroscopy alone; here, we focus on that which FTIR can describe, which are the frequencies of the  $Rh(CO)_2$  and Rh(CO) species, and the binding energy of the second CO\* to form Rh(CO)2 and how those metrics may be influenced by the hydration of the surface. The coincidence of the TPD and reactivity light-off suggest that the loss of CO\* from Rh(CO)<sub>2</sub> to form Rh(CO) is kinetically relevant, which is a step that our calculations seem to capture accurately.

The presence of additional H\*/OH\* groups on the  $(010)_b$  surface generally increases the frequencies of the symmetric and asymmetric stretches of Rh(CO)<sub>2</sub> below 7.92 OH nm<sup>-2</sup> (Figures 10 and 11). At very low coverage (0, 1.13, and 2.26)

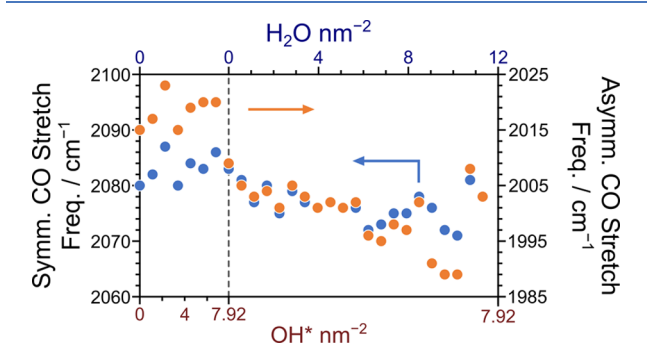


Figure 11. Changes in the symmetric (blue) and asymmetric (orange) stretches of the  $Rh(CO)_2$  with different surface concentrations of  $H^*/OH^*$  pairs and of molecular  $H_2O$  on  $\gamma$ - $Al_2O_3(010)_b$ . The coverages within which  $H_2O$  adsorbs dissociatively to form  $H^*/OH^*$  pairs (in OH nm<sup>-2</sup>) and molecularly (in  $H_2O$  nm<sup>-2</sup>) are labeled along the bottom and top ordinate, respectively.

OH nm<sup>-2</sup>), the symmetric stretch frequency increases from 2080 to 2082 and 2087 cm<sup>-1</sup> and asymmetric from 2017 to 2025 and 2027 cm<sup>-1</sup>, respectively. This trend breaks at 7.92 OH nm<sup>-2</sup>; at this coverage, Rh(CO)<sub>2</sub> rotates such that Rh<sub>1</sub> coordinates only to one surface O atom and subsequent H<sub>2</sub>O adsorption occurs molecularly (Figure 10e–f). This configurational shift causes both the symmetric and asymmetric stretching frequencies to decrease despite the increase in  $\theta_{\rm W}$  (Figure 11). As H<sub>2</sub>O continues to adsorb, the symmetric and asymmetric frequencies further decrease to lower bounds of 2071 and 1989 cm<sup>-1</sup>, respectively, at 7.92 OH nm<sup>-2</sup> and 10.18 H<sub>2</sub>O nm<sup>-2</sup>. While it is unlikely that the entire  $\gamma$ -Al<sub>2</sub>O<sub>3</sub> surface reaches this level of hydroxylation, the heterogeneity of  $\gamma$ -

 $Al_2O_3$  and likelihood of attractive OH–OH interactions suggest that OH\* could aggregate to form these high coverage regimes under the probed experimental conditions. Notably, this shift in CO\* frequency as  $\gamma$ -Al<sub>2</sub>O<sub>3</sub> reaches high  $\theta_W$  is of similar magnitude to the decrease in CO\* frequency observed in IR spectra during TPD (2094 and 2020 to 2084 and 2010 cm<sup>-1</sup>).

Changes in the Rh(CO) frequencies trend differently than those for the  $Rh(CO)_2$  with  $\theta_W$ . When only one  $CO^*$  is adsorbed, the Rh<sub>1</sub> can coordinate to two OH\* on the surface, which reduces the stretching frequency of the CO\* from 1978 cm<sup>-1</sup> with only the OH ligand to 1957 cm<sup>-1</sup> at 2.26 OH nm<sup>-2</sup> (the OH ligand with an additional dissociated H2O on y-Al<sub>2</sub>O<sub>3</sub>). After introducing this additional OH\* from an H\*/ OH\* pair to which the Rh<sub>1</sub> bonds at 2.26 OH nm<sup>-2</sup>, the CO\* frequency increases with higher OH\* coverages, increasing to 1958–1985 cm<sup>-1</sup> at  $\theta_{\rm W}$  coverages between 1.70 and 7.92 OH nm<sup>-2</sup>. Similar to that of Rh(CO)<sub>2</sub>, the frequencies of Rh(CO) begin to decrease once molecular  $H_2O$  begins adsorbing on  $\gamma$ -Al<sub>2</sub>O<sub>3</sub>, dropping from 1985 to 1962 cm<sup>-1</sup> when the first H<sub>2</sub>O adsorbs molecularly (Figure 10k). Such changes again implicate denser OH\* adlayers as a possible cause for increases in stretching frequencies despite Rh(CO) occupying less space on the support than Rh(CO)<sub>2</sub>. Finally, QUAMBO-calculated charges are relatively insensitive to OH concentration for the  $Rh(CO)_2$ , remaining between +0.55 and +0.59 e until the  $Rh(CO)_2$  rearranges at 7.92 OH nm<sup>-2</sup> coverage, when the charge drops to +0.44 e.

In summary, DFT predicts that increasing local  $\theta_{\rm W}$  around HO–Rh(CO) $_2$  can increase CO\* frequencies by ~7 cm<sup>-1</sup> from 2080/2015 cm<sup>-1</sup> at 0 OH nm<sup>-2</sup> to 2086/2020 cm<sup>-1</sup> at 6.79 OH nm<sup>-2</sup>, after which they significantly decrease to as low as 2071/1989 cm<sup>-1</sup> at 7.92 OH nm<sup>-2</sup> and 10.18 H<sub>2</sub>O nm<sup>-2</sup>. These shifts are similar to the 10 cm<sup>-1</sup> range observed in FTIR spectroscopy and decrease CO binding energies. This approach also predicts that the  $\gamma$ -Al<sub>2</sub>O<sub>3</sub> facet affects CO\* frequency of Rh(CO)<sub>2</sub>, directly through Rh-support inter-

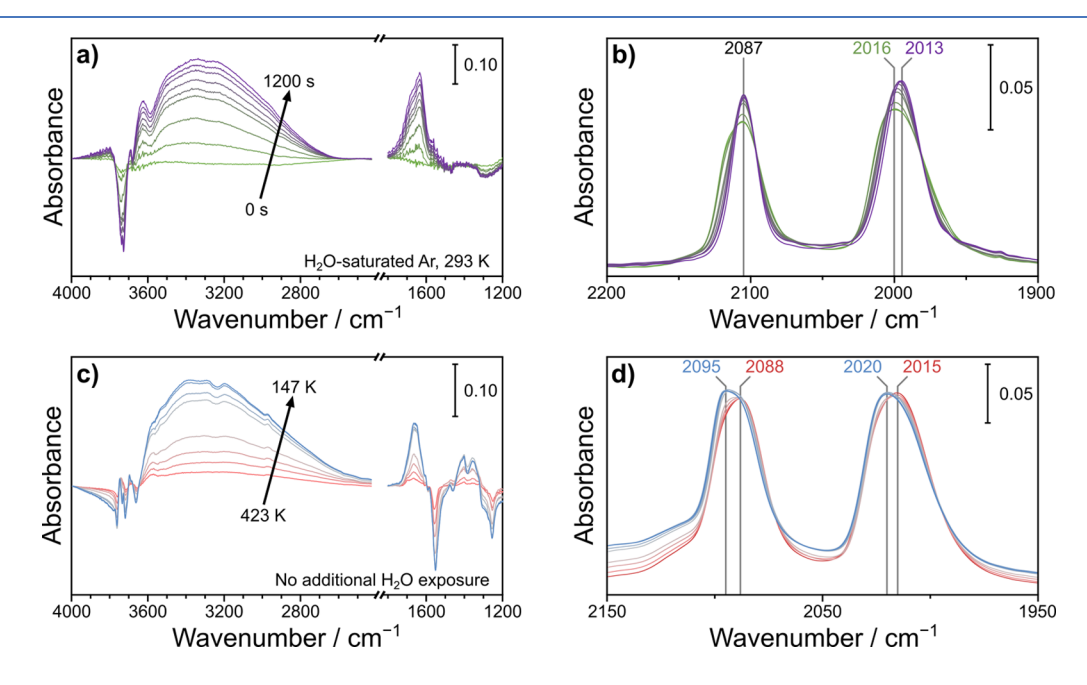


Figure 12. FTIR spectra of 0.1 wt %  $Rh/\gamma$ - $Al_2O_3$  (a,b) saturated with CO at 298 K and exposed to a water-saturated Ar stream at 298 K for 1200 s and (c,d) saturated with CO at 423 K and cooled to 147 K, highlighting the O-H stretch and H-O-H bending regions in (a,c) and the  $Rh(CO)_2$  stretch region in (b,d).

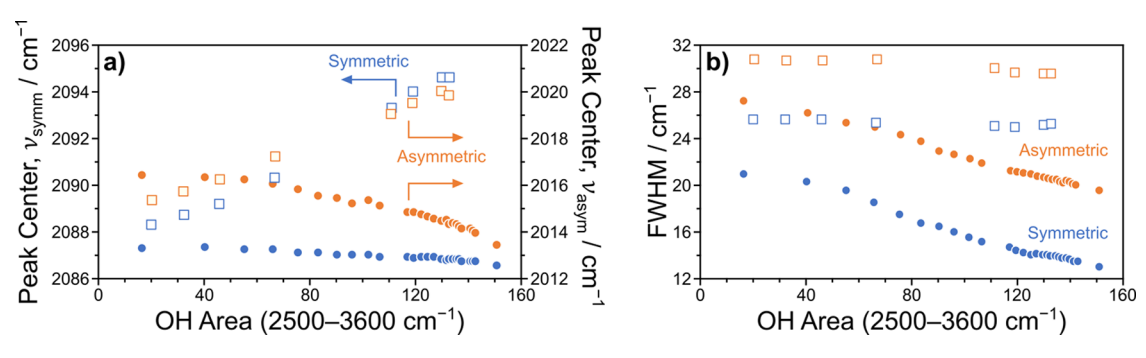


Figure 13. (a) Peak center and (b) fwhm of  $Rh(CO)_2$  peaks as the area of the OH band changes for symmetric (blue) and asymmetric (orange) stretches in samples brought to cryogenic temperatures ( $\blacksquare$ , hollow) and exposed to  $H_2O$  at 298 K ( $\blacksquare$ , filled).

actions but also indirectly by equilibrium  $\theta_W$ . Therefore, we investigate the effect of  $\theta_W$  on CO\* frequency using FTIR spectroscopy next.

Exposing 0.1 wt % Rh/ $\gamma$ -Al<sub>2</sub>O<sub>3</sub> first saturated with CO to form Rh(CO)<sub>2</sub> to an Ar feed saturated with H<sub>2</sub>O at 293 K increases the surface hydroxylation of  $\gamma$ -Al<sub>2</sub>O<sub>3</sub> (Figure 12a). This increase in  $\theta_{\mathrm{W}}$  is evidenced by the loss of isolated OH groups (>3700 cm<sup>-1</sup>)<sup>30,109,110</sup> and growth of the broad hydrogen bonding OH band from 3600 to 2500 cm<sup>-1</sup>, 30,42 indicating the formation of OH-dense regions on γ-Al<sub>2</sub>O<sub>3</sub> (Figure 12a). The growth of the H-O-H bending band at 1650 cm<sup>-1</sup> also indicates the presence of molecularly adsorbed water (Figure 12a).<sup>42</sup> Water exposure noticeably tightens the bands (~8 cm<sup>-1</sup> reduction of fwhm) around centers at 2087/ 2013 cm<sup>-1</sup> as OH\* density increases (Figures 12b and 13b), thus causing the peak centers to decrease. The reduction of the fwhm is likely because physisorbed water molecules near Rh<sub>1</sub> sites homogenize the local coordination environment, indicating that the lower frequency Rh(CO)<sub>2</sub> species with peaks near 2087 and 2013 cm<sup>-1</sup> formed during H<sub>2</sub>O exposure exist in a highly hydroxylated environment.

Separately, 0.1 wt % Rh/ $\gamma$ -Al<sub>2</sub>O<sub>3</sub> was exposed to 10 kPa CO at 423 K to form Rh(CO)<sub>2</sub> and cooled to 147 K (Figure 12c,d). The  $Rh(CO)_2$  bands initially appear similar in shape and position after CO adsorption to those at 423 K during TPD, but cooling to 147 K induces a shift in maximum intensity from 2088/2015 to 2095/2020 cm<sup>-1</sup> for the Rh(CO)<sub>2</sub> peaks—the reverse effect of heating during TPD, indicating that the conversion between Rh(CO)<sub>2</sub> species observed during TPD prior to desorption is reversible. During cooling, the hydrogen bonding OH\* region and the H-O-H bending peak (1650 cm<sup>-1</sup>) grow, indicating that trace water in the Ar feed adsorbs on the  $\gamma$ -Al<sub>2</sub>O<sub>3</sub> during cooling. This H<sub>2</sub>O adsorption does not cause as substantial a loss of isolated OH\* groups (3800-3700 cm<sup>-1</sup>) as observed during water exposure at room temperature, which presumably consumes most isolated OH\* by condensing water on the surface. Assuming that water molecularly adsorbs only on OH-saturated surfaces because of hydrogen bonding, the persistence of isolated OH\* groups suggests that during cooling to cryogenic temperatures, water preferentially deposits onto some regions of  $\gamma$ -Al<sub>2</sub>O<sub>3</sub>, leaving other regions drier. Despite increasing absorbance in the OH\* region, the fwhm of each CO\* peak does not tighten and the positions of maximum intensity of the CO\* peaks shift to higher frequencies during cooling, opposite to the behavior observed when water was fed at room temperature (Figure 13). This can be explained by OH\*-OH\* interactions on the support: at low temperature, densely packed OH\* form ice-like

layers on  $\gamma$ -Al<sub>2</sub>O<sub>3</sub> from which Rh(CO)<sub>2</sub> is excluded by the strengthening hydrogen bonding networks. Whether this exclusion occurs by Rh<sub>1</sub> migration out of dense OH\* regions or by OH\* agglomeration away from Rh(CO)<sub>2</sub> is unclear. Altogether, these results suggest that  $\theta_W$  indeed alters the frequency of CO bound to Rh<sub>1</sub>, as DFT predicts, and that the effects are moderated by temperature.

DFT also predicts that the second CO binding enthalpy  $(\Delta H_{\text{CO},2})$  weakens from -167 to -122 kJ  $\text{mol}^{-1}$  as the coverage of H\*/OH\* pairs and molecular H<sub>2</sub>O increase, suggesting that CO desorption from HO–Rh(CO)<sub>2</sub> occurs more readily in high  $\theta_{\text{W}}$  environments rather than low. The facet supporting HO–Rh(CO)<sub>2</sub> also affects CO frequency, both directly through Rh-support interactions and indirectly by equilibrium  $\theta_{\text{W}}$ . For instance, HO–Rh(CO)<sub>2</sub> on dehydrated  $(001)_{\text{b}}$  has frequencies of 2090 and 2020 cm<sup>-1</sup>, and the  $(001)_{\text{b}}$  facet retains fewer OH than the  $(010)_{\text{b}}$  or  $(100)_{\text{b}}$  facets.  $^{38,39}$  The facet dependence of  $\theta_{\text{W}}$  and the likeliness of OH\*–OH\* interactions may lead to distinct patches of high and low  $\theta_{\text{W}}$  on  $\gamma$ -Al<sub>2</sub>O<sub>3</sub> rather than a continuous distribution, which would lead to the appearance of the two relatively distinct sets of Rh(CO)<sub>2</sub> observed in FTIR.

Taken together, these data indicate that  $Rh(CO)_2$  is in the +1 state, coordinated to charge-balancing OH, and present on  $\gamma$ -Al<sub>2</sub>O<sub>3</sub> surfaces in areas of varying  $\theta_W$ . At ambient conditions,  $HO-Rh(CO)_2$  exists in heterogeneous areas of the support that contain a range of  $\theta_W$ , leading to broad and nonsymmetric CO\* stretching bands, and as temperature increases, these  $HO-Rh(CO)_2$  species migrate to more hydroxylated regions of  $\gamma$ -Al<sub>2</sub>O<sub>3</sub> (conversion of 2094/2020 cm<sup>-1</sup> bands to 2084/2010 cm<sup>-1</sup> bands). Sequential CO desorption then occurs from these  $HO-Rh(CO)_2$  species in high hydroxyl coverage regions to form a Rh(CO) species with a CO\* band in the range 1985–1975 cm<sup>-1</sup>. Thus, we propose that Rh(CO) species form in high  $\theta_W$  regions, which are the likely active site models for the CO–NO reaction on  $Rh_1$ .

# 4. CONCLUSIONS

Our combined theoretical and experimental approach rigorously characterizes atomically dispersed  $Rh_1/\gamma\text{-}Al_2O_3$  to enable mechanistic investigations of NO reduction. CO probemolecule FTIR spectroscopy on low weight-loading (0.05–0.1 wt %)  $Rh/\gamma\text{-}Al_2O_3$  catalysts shows distinct peaks at ~2090 and ~2015 cm $^{-1}$ , corresponding to symmetric and asymmetric vibrations of atomically dispersed  $Rh(CO)_2$ . At least two  $Rh(CO)_2$  species exist on  $\gamma\text{-}Al_2O_3$  at ambient temperature with CO stretching bands at 2094/2020 and 2084/2010 cm $^{-1}$ . The 2094/2020 cm $^{-1}$  species convert to those at 2084/2010 cm $^{-1}$ 

as temperature increases, after which CO desorption occurs from the lower frequency  $Rh(CO)_2$  species to form intermediate Rh(CO) with frequencies at 1985–1975 cm<sup>-1</sup>. The conversion of lower frequency  $Rh(CO)_2$  to Rh(CO) coincides with light-off in the NO–CO reaction. Characterizing this conversion process and the  $Rh(CO)_2$  species at 2084 and 2010 cm<sup>-1</sup> is therefore critical to modeling NO reduction over  $Rh_1$  active sites.

DFT calculations for Rh<sub>1</sub> on  $\gamma$ -Al<sub>2</sub>O<sub>3</sub> are complicated by the presence of multiple  $\gamma$ -Al<sub>2</sub>O<sub>3</sub> facets, charge-balancing ligands that can coordinate to Rh, and the local hydroxyl concentration on  $\gamma$ -Al<sub>2</sub>O<sub>3</sub>. We computed the CO binding energies and frequencies for Rh(CO) and Rh(CO)<sub>2</sub> on three  $\gamma$ -Al<sub>2</sub>O<sub>3</sub> surfaces on a previously developed model of  $\gamma$ -Al<sub>2</sub>O<sub>3</sub> from boehmite:  $^{35,37,38}$  (010)<sub>b</sub>, (100)<sub>b</sub>, and (001)<sub>b</sub>. We also studied Rh(CO) and Rh(CO)<sub>2</sub> surface species with various water-derived ligands: H, O, OH, O + OH, and 2OH. These ligands alter the oxidation state of Rh(CO) and Rh(CO)<sub>2</sub> and, in turn, the binding energies of CO\* and the corresponding C–O stretch frequencies. Results suggest that Rh(CO)<sub>2</sub> with the Rh in a +1 oxidation state and bound to a charge-compensating OH<sup>-</sup> ligand supported on a (010)<sub>b</sub> surface is most consistent with the experimental FTIR and TPD data.

Critically, the local OH\* concentration affects the stretching frequencies of Rh(CO)<sub>2</sub>. At OH\* coverages above 7.4 OH nm<sup>-2</sup>, the nearby OH\* groups disrupt one of the bonds of the Rh to surface O atoms. This disruption decreases Rh(CO)<sub>2</sub> symmetric and asymmetric stretching frequencies from a maximum of 2087 and 2023 cm<sup>-1</sup> at 2.26 OH nm<sup>-2</sup> to 2083 and 2009 cm<sup>-1</sup> at 7.92 OH nm<sup>-2</sup>. Experimentally observed Rh(CO)<sub>2</sub> frequencies substantially tighten around 2086/2014 cm<sup>-1</sup> when 0.1 wt % Rh<sub>1</sub>/ $\gamma$ -Al<sub>2</sub>O<sub>3</sub> is exposed to a watersaturated Ar stream at 298 K, confirming that Rh(CO), frequencies red-shift in high OH\* coverage environments. Alternatively, CO\* frequencies blue-shift when Rh(CO)<sub>2</sub> is cooled from 423 to 147 K, likely because ice-like high OH\* coverage areas exclude Rh(CO)<sub>2</sub> to areas of predominantly low OH\* coverage. DFT also predicts that CO\* desorption occurs more readily from Rh(CO)<sub>2</sub> in high OH\* coverage areas. DFT suggests that these shifts in frequency do not correspond to a change in the oxidation state of the Rh(CO)<sub>2</sub> but only in changes to the local environment around the catalyst active site. While γ-Al<sub>2</sub>O<sub>3</sub> in aged TWC converts to more thermodynamically stable phases, we believe that the effects of these OH\* coverages are important to consider for any Al<sub>2</sub>O<sub>3</sub> that can accommodate surface hydroxyls on which Rh is atomically dispersed.

This combined theoretical and experimental approach uses rigorous DFT calculations of binding enthalpies and free energies with corresponding frequencies in conjunction with probe molecule FTIR spectroscopy and temperature-programmed experiments to identify the structure of Rh<sub>1</sub> on  $\gamma$ -Al<sub>2</sub>O<sub>3</sub> under conditions consistent with NO reduction by CO. We conclude that CO\* desorption from atomically dispersed Rh<sub>1</sub>/ $\gamma$ -Al<sub>2</sub>O<sub>3</sub> occurs from Rh(CO)<sub>2</sub> bound to an OH ligand with additional OH\* nearby on the support. NO reduction occurs after desorption of CO\* from these Rh(CO)<sub>2</sub> species and interaction of NO with the now unsaturated Rh<sub>1</sub> sites, so the Rh(CO)<sub>2</sub> model presented here can be applied to future mechanistic studies of NO reduction.

#### ASSOCIATED CONTENT

# **Supporting Information**

The Supporting Information is available free of charge at https://pubs.acs.org/doi/10.1021/acscatal.2c02813.

Details of statistical mechanics treatments for calculating free energies and enthalpies, additional information about  $\gamma\text{-Al}_2\text{O}_3$  models tested in this work, IR spectra used to identify NCO\*, IR spectra of cooled Rh/ $\gamma\text{-Al}_2\text{O}_3$  samples after TPD, DFT-calculated structures with different H<sub>2</sub>O content, and additional images of DFT-calculated Rh structures with different ligands and on different  $\gamma\text{-Al}_2\text{O}_3$  surfaces (PDF)

#### AUTHOR INFORMATION

# **Corresponding Authors**

Phillip Christopher – Department of Chemical Engineering, University of California Santa Barbara, Santa Barbara, California 93106, United States; orcid.org/0000-0002-4898-5510; Email: pchristopher@ucsb.edu

David Hibbitts — Department of Chemical Engineering, University of Florida, Gainesville, Florida 32611, United States; Ocid.org/0000-0001-8606-7000; Email: hibbitts@che.ufl.edu

#### **Authors**

Alexander J. Hoffman — Department of Chemical Engineering, University of Florida, Gainesville, Florida 32611, United States; orcid.org/0000-0002-1337-9297

Chithra Asokan – Department of Chemical Engineering, University of California Santa Barbara, Santa Barbara, California 93106, United States

Nicholas Gadinas — Department of Chemical Engineering, University of California Santa Barbara, Santa Barbara, California 93106, United States

Emily Schroeder – Department of Chemical Engineering, University of California Santa Barbara, Santa Barbara, California 93106, United States

**Gregory Zakem** – Department of Chemical Engineering, University of California Santa Barbara, Santa Barbara, California 93106, United States

Steven V. Nystrom — Department of Chemical Engineering, University of Florida, Gainesville, Florida 32611, United States

Andrew "Bean" Getsoian — Research and Advanced Engineering, Ford Motor Company, Dearborn, Michigan 48124, United States; © orcid.org/0000-0003-1534-3818

Complete contact information is available at: https://pubs.acs.org/10.1021/acscatal.2c02813

## **Author Contributions**

A.J.H. and C.A. contributed equally to this work.

#### Notes

The authors declare no competing financial interest. While this article is believed to contain correct information, Ford Motor Company (Ford) does not expressly or impliedly warrant, nor assume any responsibility, for the accuracy, completeness, or usefulness of any information, apparatus, product, or process disclosed, nor represent that its use would not infringe the rights of third parties. Reference to any commercial product or process does not constitute its endorsement. This article does not provide financial, safety, medical, consumer product, or public policy advice or

recommendation. Readers should independently replicate all experiments, calculations, and results. The views and opinions expressed are of the authors and do not necessarily reflect those of Ford. This disclaimer may not be removed, altered, superseded, or modified without prior Ford permission.

## ACKNOWLEDGMENTS

This work was made possible by funding from the National Science Foundation under grant number CBET-1803165 (D.H.) and CBET-1804128 (P.C.). Computational resources were provided by Extreme Sciences and Engineering Discovery Environment (XSEDE), which is supported by the National Science Foundation grant number ACI-1548562, through allocation CTS160041, and from the University of Florida Research Computing.

#### REFERENCES

- (1) US Environmental Protection Agency. National Air Quality: Status and Trends of Key Air Pollutants https://www.epa.gov/air-trends/air-quality-national-summary (accessed on Nov 18, 2020).
- (2) Kean, A. J.; Harley, R. A.; Littlejohn, D.; Kendall, G. R. On-Road Measurement of Ammonia and Other Motor Vehicle Exhaust Emissions. *Environ. Sci. Technol.* **2000**, *34*, 3535–3539.
- (3) Getsoian, A.; Theis, J. R.; Paxton, W. A.; Lance, M. J.; Lambert, C. K. Remarkable improvement in low temperature performance of model three-way catalysts through solution atomic layer deposition. *Nat. Catal.* **2019**, *2*, 614–622.
- (4) Taylor, K. C. Nitric oxide catalysis in automotive exhaust systems. *Catal. Rev.* **1993**, *35*, 457–481.
- (5) Shelef, M.; Graham, G. W. Why Rhodium in Automotive Three-Way Catalysts? Catal. Rev. 1994, 36, 433–457.
- (6) Kravchenko, P.; Krishnan, V.; Hibbitts, D. Mechanism and Effects of Coverage and Particle Morphology on Rh-Catalyzed NO–H<sub>2</sub> Reactions. *J. Phys. Chem. C* **2020**, *124*, 13291–13303.
- (7) Hibbitts, D. D.; Jiménez, R.; Yoshimura, M.; Weiss, B.; Iglesia, E. Catalytic NO activation and NO-H<sub>2</sub> reaction pathways. *J. Catal.* **2014**, *319*, 95-109.
- (8) Rood, S.; Eslava, S.; Manigrasso, A.; Bannister, C. Recent advances in gasoline three-way catalyst formulation: A review. *Proc. Inst. Mech. Eng.*—Part D J. Automob. Eng. **2020**, 234, 936—949.
- (9) Zhang, S.; Tang, Y.; Nguyen, L.; Zhao, Y.-F.; Wu, Z.; Goh, T.-W.; Liu, J. J.; Li, Y.; Zhu, T.; Huang, W.; Frenkel, A. I.; Li, J.; Tao, F. F. Catalysis on singly dispersed Rh atoms anchored on an inert support. *ACS Catal.* **2017**, *8*, 110–121.
- (10) Roscioni, O. M.; Dyke, J. M.; Evans, J. Structural Characterization of Supported  $Rh^1(CO)_2/\gamma$ - $Rl_2O_3$  Catalysts by Periodic DFT Calculations. *J. Phys. Chem. C* **2013**, *117*, 19464.
- (11) Cavanagh, R. R.; Yates, J. T. Site distribution studies of Rh supported on  $Al_2O_3$ —An infrared study of chemisorbed CO. *J. Chem. Phys.* **1981**, 74, 4150–4155.
- (12) Yates, J. T.; Kolasinski, K. Infrared spectroscopic investigation of the rhodium gem-dicarbonyl surface species. *J. Chem. Phys.* **1983**, 79, 1026–1030.
- (13) Van't Blik, H. F. J.; Van Zon, J. B. A. D.; Huizinga, T.; Vis, J. C.; Koningsberger, D. C.; Prins, R. Structure of rhodium in an ultradispersed rhodium/alumina catalyst as studied by EXAFS and other techniques. *J. Am. Chem. Soc.* **1985**, *107*, 3139–3147.
- (14) Suzuki, A.; Inada, Y.; Yamaguchi, A.; Chihara, T.; Yuasa, M.; Nomura, M.; Iwasawa, Y. Time scale and elementary steps of CO-induced disintegration of surface rhodium clusters. *Angew. Chem., Int. Ed.* **2003**, 42, 4795–4799.
- (15) Dent, A. J.; Evans, J.; Fiddy, S. G.; Jyoti, B.; Newton, M. A.; Tromp, M. Rhodium dispersion during NO/CO conversions. *Angew. Chem., Int. Ed.* **2007**, *46*, 5356–5358.
- (16) Chuang, S. S. C.; Tan, C.-D. Combined infrared and mass spectrometric study of reactions of adsorbed NO and CO on 0.5 wt% Rh/SiO<sub>2</sub> catalyst. *Catal. Today* **1997**, *35*, 369–377.

- (17) Goldsmith, B. R.; Sanderson, E. D.; Ouyang, R.; Li, W.-X. CO-and NO-Induced Disintegration and Redispersion of Three-Way Catalysts Rhodium, Palladium, and Platinum: An ab Initio Thermodynamics Study. *J. Phys. Chem. C* **2014**, *118*, 9588–9597.
- (18) Ouyang, R.; Liu, J.-X.; Li, W.-X. Atomistic theory of Ostwald ripening and disintegration of supported metal particles under reaction conditions. *J. Am. Chem. Soc.* **2013**, *135*, 1760–1771.
- (19) Tang, Y.; Asokan, C.; Xu, M.; Graham, G. W.; Pan, X.; Christopher, P.; Li, J.; Sautet, P. Rh single atoms on TiO2 dynamically respond to reaction conditions by adapting their site. *Nat. Commun.* **2019**, *10*, 4488.
- (20) Asokan, C.; Thang, H. V.; Pacchioni, G.; Christopher, P. Reductant composition influences the coordination of atomically dispersed Rh on anatase TiO<sub>2</sub>. *Catal. Sci. Technol.* **2020**, *10*, 1597–1601.
- (21) Asokan, C.; Yang, Y.; Dang, A.; Getsoian, A.; Christopher, P. Low-Temperature Ammonia Production during NO Reduction by CO Is Due to Atomically Dispersed Rhodium Active Sites. *ACS Catal.* **2020**, *10*, 5217–5222.
- (22) Qi, J.; Christopher, P. Atomically Dispersed Rh Active Sites on Oxide Supports with Controlled Acidity for Gas-Phase Halide-Free Methanol Carbonylation to Acetic Acid. *Ind. Eng. Chem. Res.* **2019**, 58, 12632–12641.
- (23) Chow, J. C.; Watson, J. G.; Fujita, E. M.; Lu, Z.; Lawson, D. R.; Ashbaugh, L. L. Temporal and spatial variations of PM2.5 and PM10 aerosol in the Southern California air quality study. *Atmos. Environ.* 1994, 28, 2061–2080.
- (24) Khivantsev, K.; Vargas, C. G.; Tian, J.; Kovarik, L.; Jaegers, N. R.; Szanyi, J.; Wang, Y. Economizing on Precious Metals in Three-Way Catalysts: Thermally Stable and Highly Active Single-Atom Rhodium on Ceria for NO Abatement under Dry and Industrially Relevant Conditions. *Angew. Chem., Int. Ed.* **2021**, *60*, 391–398.
- (25) Van't Blik, H. F. J.; Van Zon, J. B. A. D.; Huizinga, T.; Vis, J. C.; Koningsberger, D. C.; Prins, R. An extended x-ray absorption fine structure spectroscopy study of a highly dispersed rhodium/aluminum oxide catalyst: the influence of carbon monoxide chemisorption on the topology of rhodium. *J. Phys. Chem.* **1983**, *87*, 2264–2267.
- (26) van Zon, J. B. A. D.; Koningsberger, D. C.; van't Blik, H. F. J.; Prins, R.; Sayers, D. E. On the detection with EXAFS of metal-support oxygen bonds in a highly dispersed rhodium on alumina catalyst. *J. Chem. Phys.* **1984**, *80*, 3914–3915.
- (27) Yang, A. C.; Garl, C. W. Infrared studies of carbon monoxide chemisorbed on rhodium. *J. Phys. Chem.* **1957**, *61*, 1504–1512.
- (28) Basu, P.; Panayotov, D.; Yates, J. T. Rhodium-carbon monoxide surface chemistry: the involvement of surface hydroxyl groups on alumina and silica supports. *J. Am. Chem. Soc.* **1988**, *110*, 2074–2081.
- (29) Newton, M. A.; Jyoti, B.; Dent, A. J.; Fiddy, S. G.; Evans, J. Synchronous, time resolved, diffuse reflectance FT-IR, energy dispersive EXAFS (EDE) and mass spectrometric investigation of the behaviour of Rh catalysts during NO reduction by CO. *Chem. Commun.* 2004, 2382–2383.
- (30) Morterra, C.; Magnacca, G. A case study: surface chemistry and surface structure of catalytic aluminas, as studied by vibrational spectroscopy of adsorbed species. *Catal. Today* **1996**, *27*, 497–532.
- (31) Busca, G. The surface of transitional aluminas: A critical review. *Catal. Today* **2014**, *226*, 2–13.
- (32) Phung, T. K.; Proietti Hernández, L.; Lagazzo, A.; Busca, G. Dehydration of ethanol over zeolites, silica alumina and alumina: Lewis acidity, Brønsted acidity and confinement effects. *Appl. Catal., A* **2015**, *493*, 77–89.
- (33) Batista, A. T. F.; Baaziz, W.; Taleb, A.-L.; Chaniot, J.; Moreaud, M.; Legens, C.; Aguilar-Tapia, A.; Proux, O.; Hazemann, J.-L.; Diehl, F.; Chizallet, C.; Gay, A.-S.; Ersen, O.; Raybaud, P. Atomic Scale Insight into the Formation, Size, and Location of Platinum Nanoparticles Supported on  $\gamma$ -Alumina. *ACS Catal.* **2020**, *10*, 4193–4204.
- (34) Rozita, Y.; Brydson, R.; Scott, A. J. An investigation of commercial gamma-Al<sub>2</sub> O<sub>3</sub> nanoparticles. *J. Phys.: Conf. Ser.* **2010**, 241, 012096.

- (35) Digne, M.; Sautet, P.; Raybaud, P.; Euzen, P.; Toulhoat, H. Use of DFT to achieve a rational understanding of acid—basic properties of  $\gamma$ -alumina surfaces. *J. Catal.* **2004**, 226, 54—68.
- (36) Raybaud, P.; Chizallet, C.; Mager-Maury, C.; Digne, M.; Toulhoat, H.; Sautet, P. From γ-alumina to supported platinum nanoclusters in reforming conditions: 10years of DFT modeling and beyond. *J. Catal.* **2013**, 308, 328–340.
- (37) Krokidis, X.; Raybaud, P.; Gobichon, A.-E.; Rebours, B.; Euzen, P.; Toulhoat, H. Theoretical Study of the Dehydration Process of Boehmite to γ-Alumina. *J. Phys. Chem. B* **2001**, *105*, 5121–5130.
- (38) Digne, M.; Sautet, P.; Raybaud, P.; Euzen, P.; Toulhoat, H. Hydroxyl Groups on  $\gamma$ -Alumina Surfaces: A DFT Study. *J. Catal.* **2002**, *211*, 1–5.
- (39) Pigeon, T.; Chizallet, C.; Raybaud, P. Revisiting  $\gamma$ -alumina surface models through the topotactic transformation of boehmite surfaces. *J. Catal.* **2022**, *405*, 140–151.
- (40) McHale, J. M.; Auroux, A.; Perrotta, A. J.; Navrotsky, A. Surface energies and thermodynamic phase stability in nanocrystalline aluminas. *Science* **1997**, 277, 788–791.
- (41) Hietala, J.; Root, A.; Knuuttila, P. The Surface Acidity of Pure and Modified Aluminas in Re/Al<sub>2</sub>O<sub>3</sub> Metathesis Catalysts as Studied by <sup>1</sup>H MAS NMR Spectroscopy and Its Importance in the Ethenolysis of 1,5-Cyclooctadiene. *J. Catal.* **1994**, *150*, 46–55.
- (42) Al-Abadleh, H. A.; Grassian, V. H. FT-IR Study of Water Adsorption on Aluminum Oxide Surfaces. *Langmuir* **2003**, *19*, 341–347
- (43) Chiche, D.; Chizallet, C.; Durupthy, O.; Chanéac, C.; Revel, R.; Raybaud, P.; Jolivet, J.-P. Growth of boehmite particles in the presence of xylitol: morphology oriented by the nest effect of hydrogen bonding. *Phys. Chem. Chem. Phys.* **2009**, *11*, 11310–11323.
- (44) Wakou, B. F. N.; Valero, M. C.; Raybaud, P. Theoretical Insights into the Interaction of Oxygenated Organic Molecules and Cobalt(II) Precursor with  $\gamma$ -Al<sub>2</sub> O<sub>3</sub> Surfaces. *J. Phys. Chem. C* **2018**, 122, 19560–19574.
- (45) Paukshtis, E. A.; Yaranova, M. A.; Batueva, I. S.; Bal'zhinimaev, B. S. A FTIR study of silanol nests over mesoporous silicate materials. *Microporous Mesoporous Mater.* **2019**, 288, 109582.
- (46) Bukowski, B. C.; Bates, J. S.; Gounder, R.; Greeley, J. Defect-Mediated Ordering of Condensed Water Structures in Microporous Zeolites. *Angew. Chem., Int. Ed.* **2019**, *58*, 16422–16426.
- (47) Bregante, D. T.; Chan, M. C.; Tan, J. Z.; Ayla, E. Z.; Nicholas, C. P.; Shukla, D.; Flaherty, D. W. The shape of water in zeolites and its impact on epoxidation catalysis. *Nat. Catal.* **2021**, *4*, 797–808.
- (48) Chen, N. Y. Hydrophobic properties of zeolites. J. Phys. Chem. 1976, 80, 60–64
- (49) Li, Z.; Jiang, X.; Xiong, G.; Nie, B.; Liu, C.; He, N.; Liu, J. Towards the preparation of binderless ZSM-5 zeolite catalysts: the crucial role of silanol nests. *Catal. Sci. Technol.* **2020**, *10*, 7829–7841.
- (50) Sulpizi, M.; Gaigeot, M.-P.; Sprik, M. The Silica-Water Interface: How the Silanols Determine the Surface Acidity and Modulate the Water Properties. *J. Chem. Theory Comput.* **2012**, 8, 1037–1047.
- (51) Hucul, D. A.; Brenner, A. A strong metal-support interaction between mononuclear and polynuclear transition metal complexes and oxide supports which dramatically affects catalytic activity. *J. Phys. Chem.* **1981**, *85*, 496–498.
- (52) Paul, D. K.; Marten, C. D.; Yates, J. T. Control of Rh<sup>I</sup>(CO)<sub>2</sub> formation on Rh/Al<sub>2</sub>O<sub>3</sub> catalysts by complexation of surface –OH groups using NH<sub>3</sub>. *Langmuir* **1999**, *15*, 4508–4512.
- (53) Zakem, G.; Ro, I.; Finzel, J.; Christopher, P. Support functionalization as an approach for modifying activation entropies of catalytic reactions on atomically dispersed metal sites. *J. Catal.* **2021**, 404, 883–896.
- (54) Zhang, J.; Asokan, C.; Zakem, G.; Christopher, P.; Medlin, J. W. Enhancing Sintering Resistance of Atomically Dispersed Catalysts in Reducing Environments with Organic Monolayers; Green Energy & Environment, 2021.
- (55) Valero, M. C.; Raybaud, P.; Sautet, P. Influence of the hydroxylation of  $\gamma$ -Al<sub>2</sub>O<sub>3</sub> surfaces on the stability and diffusion of

- single Pd atoms: a DFT study. J. Phys. Chem. B 2006, 110, 1759-1767.
- (56) Kresse, G.; Furthmüller, J. Efficiency of ab-initio total energy calculations for metals and semiconductors using a plane-wave basis set. *Comput. Mater. Sci.* **1996**, *6*, 15–50.
- (57) Kresse, G.; Hafner, J. Ab initio molecular-dynamics simulation of the liquid-metal—amorphous-semiconductor transition in germanium. *Phys. Rev. B: Condens. Matter Mater. Phys.* **1994**, 49, 14251—14269.
- (58) Kresse, G.; Hafner, J. Ab initio molecular dynamics for liquid metals. *Phys. Rev. B: Condens. Matter Mater. Phys.* **1993**, 47, 558–561.
- (59) Kresse, G.; Furthmüller, J. Efficient iterative schemes for ab initio total-energy calculations using a plane-wave basis set. *Phys. Rev. B: Condens. Matter Mater. Phys.* **1996**, *54*, 11169–11186.
- (60) Kravchenko, P.; Plaisance, C.; Hibbitts, D. A new computational interface for catalysis, **2019**, Published as pre-print on https://chemrxiv.org/articles/preprint/8040737.
- (61) Hammer, B.; Hansen, L. B.; Nørskov, J. K. Improved adsorption energetics within density-functional theory using revised Perdew-Burke-Ernzerhof functionals. *Phys. Rev. B: Condens. Matter Mater. Phys.* **1999**, *59*, 7413–7421.
- (62) Perdew, J. P.; Burke, K.; Ernzerhof, M. Generalized gradient approximation made simple. *Phys. Rev. Lett.* **1996**, *77*, 3865–3868.
- (63) Kresse, G.; Joubert, D. From ultrasoft pseudopotentials to the projector augmented-wave method. *Phys. Rev. B: Condens. Matter Mater. Phys.* **1999**, *59*, 1758–1775.
- (64) Blöchl, P. E. Projector augmented-wave method. *Phys. Rev. B: Condens. Matter Mater. Phys.* **1994**, *50*, 17953–17979.
- (65) Heyd, J.; Scuseria, G. E. Efficient hybrid density functional calculations in solids: assessment of the Heyd-Scuseria-Ernzerhof screened Coulomb hybrid functional. *J. Chem. Phys.* **2004**, *121*, 1187–1192.
- (66) Krukau, A. V.; Vydrov, O. A.; Izmaylov, A. F.; Scuseria, G. E. Influence of the exchange screening parameter on the performance of screened hybrid functionals. *J. Chem. Phys.* **2006**, *125*, 224106.
- (67) Heyd, J.; Scuseria, G. E.; Ernzerhof, M. Hybrid functionals based on a screened Coulomb potential. *J. Chem. Phys.* **2003**, *118*, 8207–8215.
- (68) Heyd, J.; Scuseria, G. E.; Ernzerhof, M. Erratum: "Hybrid functionals based on a screened Coulomb potential" [J. Chem. Phys. 118, 8207 (2003)]. J. Chem. Phys. 2006, 124, 219906.
- (69) Qian, X.; Li, J.; Qi, L.; Wang, C.-Z.; Chan, T.-L.; Yao, Y.-X.; Ho, K.-M.; Yip, S. Quasiatomic orbitals for ab initio tight-binding analysis. *Phys. Rev. B: Condens. Matter Mater. Phys.* **2008**, 78, 245112.
- (70) Gutiérrez, G.; Taga, A.; Johansson, B. Theoretical structure determination of  $\gamma$ -Al<sub>2</sub>O<sub>3</sub>. *Phys. Rev. B: Condens. Matter Mater. Phys.* **2001**, *65*, 012101.
- (71) McQuarrie, D. A. Statistical Mechanics; University Science Books: Sausalito, Calif, 2000.
- (72) Almithn, A.; Hibbitts, D. Effects of catalyst model and high adsorbate coverages in ab initio studies of alkane hydrogenolysis. *ACS Catal.* **2018**. *8*. 6375–6387.
- (73) Almithn, A. S.; Hibbitts, D. D. Impact of metal and heteroatom identities in the hydrogenolysis of C-X bonds (X = C, X = C, X
- (74) NIST. Chemistry WebBook, NIST Standard Reference Database Number 69; Linstrom, P. J.; Mallard, W. G., Eds.; National Institute of Standards and Technology: Gaithersburg MD, 2020.
- (75) Redhead, P. A. Thermal desorption of gases. Vacuum 1962, 12, 203–211.
- (76) Campbell, C. T.; Sellers, J. R. V. The entropies of adsorbed molecules. J. Am. Chem. Soc. 2012, 134, 18109–18115.
- (77) Hoffman, A. J.; Asokan, C.; Gadinas, N.; Kravchenko, P.; Getsoian, A.; Christopher, P.; Hibbitts, D. Theoretical and Experimental Characterization of Adsorbed CO and NO on  $\gamma$ -Al<sub>2</sub>O<sub>3</sub>-Supported Rh Nanoparticles. *J. Phys. Chem. C* **2021**, *125*, 19733–19755.

- (78) Yoo, C.-J.; Getsoian, A.; Bhan, A. NH<sub>3</sub> formation pathways from NO reduction by CO in the presence of water over Rh/Al<sub>2</sub>O<sub>3</sub>. *Appl. Catal., B* **2021**, 286, 119893.
- (79) Solymosi, F.; Bansagi, T. Infrared spectroscopic study of the adsorption of isocyanic acid. *J. Phys. Chem.* **1979**, 83, 552–553.
- (80) Solymosi, F.; Sárkány, J. An infrared study of the surface interaction between NO and CO on Rh/Al<sub>2</sub>O<sub>3</sub> catalyst. *Appl. Surf. Sci.* **1979**, *3*, 68–82.
- (81) Solymosi, F.; Völgyesi, L.; Raskó, J. The effects of different supports on the formation and reactivity of surface isocyanate on Pd, Ir, Ru and Rh. Z. Phys. Chem. 1980, 120, 79–87.
- (82) Solymosi, F.; Völgyesi, L.; Sárkány, J. The effect of the support on the formation and stability of surface isocyanate on platinum. *J. Catal.* **1978**, *54*, 336–344.
- (83) Doherty, F.; Goldsmith, B. R. Rhodium single-atom catalysts on titania for reverse water gas shift reaction explored by first principles mechanistic analysis and compared to nanoclusters. *ChemCatChem* **2021**, *13*, 3155–3164.
- (84) Thang, H. V.; Pacchioni, G. On the real nature of Rh single-atom catalysts dispersed on the ZrO<sub>2</sub> surface. *ChemCatChem* **2020**, 12, 2595–2604.
- (85) Paolucci, C.; Parekh, A. A.; Khurana, I.; Di Iorio, J. R.; Li, H.; Albarracin Caballero, J. D.; Shih, A. J.; Anggara, T.; Delgass, W. N.; Miller, J. T.; Ribeiro, F. H.; Gounder, R.; Schneider, W. F. Catalysis in a Cage: Condition-Dependent Speciation and Dynamics of Exchanged Cu Cations in SSZ-13 Zeolites. *J. Am. Chem. Soc.* **2016**, 138, 6028–6048.
- (86) Anggara, T.; Paolucci, C.; Schneider, W. F. Periodic DFT Characterization of NO<sub>x</sub> Adsorption in Cu-Exchanged SSZ-13 Zeolite Catalysts. *J. Phys. Chem. C* **2016**, *120*, 27934–27943.
- (87) Paolucci, C.; Verma, A. A.; Bates, S. A.; Kispersky, V. F.; Miller, J. T.; Gounder, R.; Delgass, W. N.; Ribeiro, F. H.; Schneider, W. F. Isolation of the copper redox steps in the standard selective catalytic reduction on Cu-SSZ-13. *Angew. Chem., Int. Ed.* **2014**, *53*, 11828–11833.
- (88) Mandal, K.; Gu, Y.; Westendorff, K. S.; Li, S.; Pihl, J. A.; Grabow, L. C.; Epling, W. S.; Paolucci, C. Condition-Dependent Pd Speciation and NO Adsorption in Pd/Zeolites. *ACS Catal.* **2020**, *10*, 12801–12818.
- (89) Hecker, W.; Bell, A. T. Reduction of NO by CO over silicasupported rhodium: infrared and kinetic studies. *J. Catal.* **1983**, *84*, 200–215.
- (90) Matsubu, J. C.; Yang, V. N.; Christopher, P. Isolated metal active site concentration and stability control catalytic CO<sub>2</sub> reduction selectivity. *J. Am. Chem. Soc.* **2015**, *137*, 3076–3084.
- (91) Serna, P.; Gates, B. C. Zeolite-supported rhodium complexes and clusters: switching catalytic selectivity by controlling structures of essentially molecular species. *J. Am. Chem. Soc.* **2011**, *133*, 4714–4717.
- (92) Wong, J. C. S.; Yates, J. T. Photochemical Activation of C-H Bonds on a Rhodium Catalyst. Observation of a Competitive Effect on the Surface. J. Am. Chem. Soc. 1994, 116, 1610–1615.
- (93) Fang, C.-Y.; Valecillos, J.; Conley, E. T.; Chen, C.-Y.; Castaño, P.; Gates, B. C. Synthesis of Rh<sub>6</sub>(CO)<sub>16</sub> in Supercages of Zeolite HY: Reaction Network and Kinetics of Formation from Mononuclear Rhodium Precursors via Rh<sub>4</sub>(CO)<sub>12</sub> Facilitated by the Water Gas Shift Half-Reaction. *J. Phys. Chem. C* **2020**, *124*, 2513–2520.
- (94) Schroeder, E. K.; Finzel, J.; Christopher, P. Unpublished results, 2022.
- (95) Solymosi, F.; Pasztor, M. An infrared study of the influence of carbon monoxide chemisorption on the topology of supported rhodium. *J. Phys. Chem.* **1985**, *89*, 4789–4793.
- (96) Smrcok, L.; Langer, V.; Krestan, J. γ-Alumina: a single-crystal X-ray diffraction study. *Acta Crystallogr. C* **2006**, *62*, i83.
- (97) Samain, L.; Jaworski, A.; Edén, M.; Ladd, D. M.; Seo, D.-K.; Javier Garcia-Garcia, F.; Häussermann, U. Structural analysis of highly porous γ-Al<sub>2</sub>O<sub>3</sub>. *J. Solid State Chem.* **2014**, *217*, 1–8.

- (98) Sohlberg, K.; Pennycook, S. J.; Pantelides, S. T. The bulk and the surface structure of  $\gamma$ -alumina. *Chem. Eng. Commun.* **2000**, *181*, 107-135.
- (99) Prins, R. On the structure of  $\gamma$ -Al<sub>2</sub>O<sub>3</sub>. *J. Catal.* **2020**, 392, 336–346.
- (100) Prins, R. Location of the Spinel Vacancies in  $\gamma$ -Al $_2$ O $_3$ . Angew. Chem., Int. Ed. **2019**, 58, 15548–15552.
- (101) Khivantsev, K.; Jaegers, N. R.; Kwak, J.-H.; Szanyi, J.; Kovarik, L. Precise Identification and Characterization of Catalytically Active Sites on the Surface of  $\gamma$ -Alumina\*. *Angew. Chem., Int. Ed.* **2021**, *60*, 17522–17530.
- (102) Nortier, P.; Fourre, P.; Saad, A. B. M.; Saur, O.; Lavalley, J. C. Effects of crystallinity and morphology on the surface properties of alumina. *Appl. Catal.* **1990**, *61*, 141–160.
- (103) Walsh, A.; Sokol, A. A.; Buckeridge, J.; Scanlon, D. O.; Catlow, C. R. A. Oxidation states and ionicity. *Nat. Mater.* **2018**, *17*, 958–964.
- (104) Walsh, A.; Sokol, A. A.; Buckeridge, J.; Scanlon, D. O.; Catlow, C. R. A. Electron counting in solids: oxidation states, partial charges, and ionicity. *J. Phys. Chem. Lett.* **2017**, *8*, 2074–2075.
- (105) Koch, D.; Manzhos, S. On the charge state of titanium in titanium dioxide. J. Phys. Chem. Lett. 2017, 8, 1593–1598.
- (106) Valero, M. C.; Digne, M.; Sautet, P.; Raybaud, P. DFT Study of the Interaction of a single Palladium Atom with  $\gamma$ -Alumina Surfaces: the Role of Hydroxylation. *Oil Gas Sci. Technol.* **2006**, *61*, 535–545
- (107) Saavedra, J.; Doan, H. A.; Pursell, C. J.; Grabow, L. C.; Chandler, B. D. The critical role of water at the gold-titania interface in catalytic CO oxidation. *Science* **2014**, *345*, 1599–1602.
- (108) Ojeda, M.; Zhan, B.-Z.; Iglesia, E. Mechanistic interpretation of CO oxidation turnover rates on supported Au clusters. *J. Catal.* **2012**, 285, 92–102.
- (109) Peri, J. B. A Model for the Surface of  $\gamma$ -Alumina<sup>1</sup>. *J. Phys. Chem.* **1965**, *69*, 220–230.
- (110) Tsyganenko, A. A.; Filimonov, V. N. Infrared spectra of surface hydroxyl groups and crystalline structure of oxides. *J. Mol. Struct.* **1973**, *19*, 579–589.
- (111) Towns, J.; Cockerill, T.; Dahan, M.; Foster, I.; Gaither, K.; Grimshaw, A.; Hazlewood, V.; Lathrop, S.; Lifka, D.; Peterson, G. D.; Roskies, R.; Scott, J. R.; Wilkins-Diehr, N. XSEDE: accelerating scientific discovery. *Comput. Sci. Eng.* **2014**, *16*, 62–74.